Materials Horizons

ROYAL SOCIETY OF CHEMISTRY

COMMUNICATION

View Article Online
View Journal | View Issue

Cite this: *Mater. Horiz.*, 2025, **12**, 4771

Received 26th February 2025,
Accepted 19th March 2025

DOI: 10.1039/d5mh00351b

rsc.li/materials-horizons

A switch-on chemo-photothermal nanotherapy impairs glioblastoma†

Maria Mendes,[ab] Maria António,[c] Ana L. Daniel-da-Silva,[c] José Sereno,[bde] Rui Oliveira,[fgh] Luís G. Arnaut,[b] Célia Gomes,[ehi] Maria Luísa Ramos,[b] Miguel Castelo-Branco,[de] João Sousa,[ab] Alberto Pais[b] and Carla Vitorino*[ab]

Judiciously combined modality approaches have proved highly effective for treating most forms of cancer, including glioblastoma. This study introduces a hybrid nanoparticle-based treatment designed to induce a synergistic effect. It employs repurposed celecoxib-loaded hybrid nanoparticles (HNPs) that are thermally activated by near-infrared laser irradiation to damage glioblastoma cells. The HNPs are constructed by covalently binding organic (ultra-small nanostructured lipid carriers, usNLCs) and inorganic nanoparticles (gold nanorods, AuNRs, with photothermal therapy capability), using c(RGDfK) that serves the dual purpose of a biolinker and a tumor-targeting peptide. The HNPs are further functionalized with transferrin (Tf) as a blood–brain barrier ligand denoted as HNPs^{Tf}. Our comprehensive *in vitro* and *in vivo* studies have unveiled the remarkable capability of HNPs^{Tf} to safely and specifically increase blood–brain barrier permeability through transferrin receptor interactions, facilitating precise nanoparticle accumulation in the tumor region within orthotopic tumor-bearing mice. Furthermore, the orchestrated combination of chemo- and photothermal therapy has exhibited a substantial therapeutic impact on glioblastoma, showcasing a noteworthy 78% inhibition in tumor volume growth and an impressive 98% delay in tumor growth. Notably, this treatment approach has resulted in prolonged survival rates among tumor-bearing mice, accompanied by a favorable side effect profile. Overall, our findings unequivocally demonstrate that celecoxib-loaded HNPs^{Tf} offer a game-changing, chemo-photothermal combination, unleashing a synergistic effect that significantly enhances both brain drug delivery and the efficacy of anti-glioblastoma treatments.

New concepts

This work introduces a unique hybrid lipid–gold nanoparticle (HNP) design for chemo-photothermal therapy of glioblastoma, based on a precise covalent linkage between solid lipid nanoparticles and gold nanorods, prompted by the c(RGDfK) peptide. Herein, a pivotal role is assigned to c(RGDfK), which serves both as a glioblastoma cell-targeting peptide and a biolinker between the inorganic and organic nanoparticles. HNPs are further surface-decorated with transferrin. This innovative design yields a differentiated multi-target nanosystem based on the dual blood–brain barrier (BBB)-blood–brain tumor barrier (BTBB) ligand docking approach. An additional insight is provided by the site-specific heat production induced by near-infrared brain irradiation, within a multimodal therapeutic approach.

Introduction

Glioblastoma (GB) is the most lethal primary brain tumor, and although its incidence is low compared to other cancers, 1.6% of new cancer cases, 82% of new cases result in death.[1] For patients recently diagnosed with GB, the established treatment protocol includes maximal resection, subsequent to radiotherapy over 6 weeks with concomitant temozolomide chemotherapy

[a] *Faculty of Pharmacy, University of Coimbra, Coimbra, Portugal. E-mail: csvitorino@ff.uc.pt*
[b] *Coimbra Chemistry Centre, Institute of Molecular Sciences – IMS, Department of Chemistry, University of Coimbra, 3000-535 Coimbra, Portugal*
[c] *CICECO-Aveiro Institute of Materials, Chemistry Department, University of Aveiro, 3810-193 Aveiro, Portugal*
[d] *Coimbra Institute for Biomedical Imaging and Translational Research (CIBIT), University of Coimbra, 3000-548 Coimbra, Portugal*
[e] *Institute of Nuclear Sciences Applied to Health (ICNAS), University of Coimbra, 3000-548 Coimbra, Portugal*
[f] *Coimbra Institute for Clinical and Biomedical Research (iCBR)/Center of Environmental Genetics of Oncobiology (CIMAGO), Faculty of Medicine (FMUC), University of Coimbra, 3000-548 Coimbra, Portugal*
[g] *Biophysics Institute, Faculty of Medicine, University of Coimbra, 3000-548 Coimbra, Portugal*
[h] *Germano de Sousa Pathological Anatomy Center, Quinta de Voimarães, Rua de S. Teotónio, 3000-377 Coimbra, Portugal*
[i] *Center for Innovative Biomedicine and Biotechnology Consortium (CIBB), University of Coimbra, 3000-548 Coimbra, Portugal*
† Electronic supplementary information (ESI) available. See DOI: https://doi.org/10.1039/d5mh00351b

followed by temozolomide maintenance. The midpoint period until progression is 6 months, and the overall survival ranges from 16 to 18 months. This poor prognosis is due to the location of the tumor and to its diffuse and infiltrative nature in the adjacent brain parenchyma.[2,3] For these reasons, complete surgical resection is restricted, resulting in tumor recurrence and metastasis. Other challenges associated with GB treatment include the large phenotypic and genotypic heterogeneity, which results in multidrug resistance. Furthermore, the lack of specificity of current therapies leads to significant toxicity toward healthy tissues and limited penetration through key barriers such as the blood–brain barrier (BBB) and blood–brain tumor barrier (BTB).[4–6]

Despite the implementation of a combinatory treatment approach in glioblastoma (GB), there has been no substantial improvement in patient outcomes. Consequently, the development of single drug delivery systems that integrate multiple modalities is imperative. These combined-modality therapies aim to conjugate various antitumor mechanisms to address the limitations of existing treatments. Recently, a noteworthy advancement involved the integration of chemotherapy and photothermal therapy within a single nanoparticle, resulting in an enhanced antitumor efficacy.[7,8]

Chemotherapy is an important form of cancer treatment. However, the emergence of multidrug resistance in cancer cells and the resultant systemic toxic side effects from non-specific drug delivery represent significant hurdles to success in the treatment of several cancers. Temozolomide is a clear example of a chemotherapeutic drug with low efficacy that has not significantly improved the survival rate of patients over the years. In this context, the drug repurposing approach has promising potential to identify new uses for approved drugs beyond their original medical indication and to expand the anticancer portfolio.[9,10] Drug repurposing is a rapid strategy to find an effective treatment with lower costs and risks. Celecoxib, a selective cyclooxygenase inhibitor, has been utilized for over 20 years as an anti-inflammatory, analgesic, and antipyretic drug.[11–13] In recent years, celecoxib has been highlighted as a good candidate with anti-neoplastic activity against numerous cancer types, including glioblastoma.[14,15] Preclinical data suggest that it may have a chemopreventive effect against breast cancer. More recently, the FDA approved celecoxib for the treatment of familial adenomatous polyposis to prevent the formation and growth of colon polyps.[16,17]

Photothermal therapy (PTT) stands out as an appealing approach for treating solid tumors, offering benefits over conventional therapeutic modalities, characterized by specificity, minimal invasiveness, and particular spatial-temporal selectivity. PTT involves the conversion of photon energy into cytotoxic heat, leading to the damage and eradication of cancer cells. The photothermal effect enables a localized temperature increase, causing cancer cell destruction through necrosis when the temperature reaches 50 °C, a phenomenon known as thermal ablation.[18] In contrast, a mild photothermal effect (39–45 °C) significantly amplifies the chemotherapeutic impact through thermo-sensitization. This induces damage to DNA repair, membrane integrity, improved blood flow and tumor penetration, and activation of the apoptosis mechanism.[18,19] Although several heat sources, such as ultrasound, radiofrequency, microwaves, and electromagnetic waves,[20] have been employed clinically, near-infrared (NIR) radiation has attracted special attention relative to other sources, owing to its non-invasive effect and high tissue penetration.[21–25] NIR radiation is not selectively absorbed by tumors and cannot be used alone to eradicate them. However, when a NIR absorbing material is present in the organism exposed to NIR radiation, it will be a heat source as long as it absorbs NIR radiation. For sufficiently intense NIR radiation, this heat source will trigger cell death mechanisms that bypass multidrug resistance.[26,27]

Numerous nanotechnologies have garnered significant attention for the treatment of glioblastoma (GB), particularly those employing combined modality therapy. Furthermore, there has been a substantial surge in the application of engineered hybrid nanoparticles for glioblastoma over the past few decades. Hybridization of effective treatments can enable combination therapy, leading to higher success rates in antitumor efficacy and better quality of life for patients. Moreover, appropriate tuning of particle properties to smaller sizes can enhance nanoparticle gathering within tumor tissue through the mechanism of enhanced permeability and retention (EPR).[28,29] Another important aspect is the surface modification with specific ligands, which confers active targeting capabilities to these nanoparticles and improves nanoparticle concentration at the target site, reducing their concentration in the unwanted tissue. Hybrid nanoparticles (HNPs), composed of ultra-small nanostructured lipid carriers (usNLCs) as a drug loading system and Au as a heating moiety, offer unique advantages for chemo-photothermal therapy in a single system.

usNLCs, the solid lipid-matrix NPs, represent a promising candidate carrier for glioblastoma treatment.[30–33] Their numerous advantages include their biocompatible and biodegradable nature, high encapsulation capacity, drug protection from biological effects in the bloodstream and at the target site, control over the release, suitable storage stability, and the ability for large-scale production with an excellent cost-effective ratio.[34–37] The reduced particle size (<100 nm), high specific surface area and accessible surface functionalization make usNLCs an attractive nanocarrier for drug delivery. Due to their lipophilic matrix, they can be easily loaded with celecoxib with high efficiency.

Gold nanorods (AuNRs) have attracted interest in diagnosis, drug delivery, and photothermal therapy owing to their adjustable size during synthesis, ease of surface functionalization, excellent plasmonic properties, biocompatibility, and resistance to photobleaching.[38,39] AuNRs exhibit excellent surface plasmon resonance (SPR) with the capacity to convert radiation into heat with high efficiency, as they can produce a hyperthermia effect when excited with an NIR laser. By controlling the particle size and aspect ratio during synthesis, the plasmonic resonance band can be modified to absorb in the biological window region (750–1400 nm).[20] This biological window provides increased transparency toward biological matter. In addition,

light absorption and scattering in AuNRs may be intensely enhanced, which endow them numerous therapeutic modalities, including PTT and/or photodynamic therapy.[39–43] Moreover, when combined with organic nanoparticles, they can suppress cancer cells by exerting synergistic effects and reversing drug resistance.[25,27]

HNPs gather the advantages of usNLCs, the NIR-sensitivity of AuNRs, and the active targeting ability of both. As such, they become robust nanoparticles, comprising three distinct functional components: (i) a lipophilic core designed to entrap poorly water-soluble drugs, thereby enhancing drug encapsulation efficiency and controlling drug release; (ii) an inorganic shell with photothermal capability that raises local temperatures above 39 °C under NIR irradiation; and (iii) an outer layer designed to target overexpressed transferrin receptors at the BBB, facilitating effective targeting for crossing the BBB and ultimately reaching the brain tumor.

In the present study, the design and development of targeted HNPs, combining chemo- and photothermal therapy against GB, are reported. The HNP construction relies on the covalent linkage between usNLCs and AuNRs. The active targeting strategy was implemented to warrant a specific delivery to the brain by using transferrin (which targets the BBB) and the c(RGDfK) peptide (which not only targets the GB tumor barrier but also serves as a linker between inorganic and organic nanoparticles). The c(RGDfK) is a key targeting molecule for GB cells due to its high affinity for integrins, particularly $\alpha_v\beta_3$, which are overexpressed on the surface of GB cells, enhancing selective delivery of therapeutic agents and improving treatment efficacy.[32,44–46]

The HNPs were assessed considering their physicochemical characteristics, including particle size, zeta potential, polydispersity, drug loading, and photothermal properties. The *in vitro* performance of the HNPs regarding permeability through HBMEC, cytotoxicity and cellular uptake efficiency using HBMEC and U87 cells, and cell apoptosis of U87 cells was evaluated. Finally, the *in vitro* findings were further confirmed by *in vivo* studies, such as biodistribution, efficacy studies in an orthotopic glioblastoma mouse model through magnetic resonance imaging (MRI), and toxicity evaluation.

Overall, this chemo-photothermal combination constitutes a game-changing strategy for improving brain drug delivery and anti-glioblastoma treatment efficacy.

Results and discussion

Hybrid lipid–gold nanoparticles with dual targeting for chemo-photothermal therapy against glioblastoma were developed, characterized with respect to their colloidal properties, and evaluated for the performance of the nanoparticles both *in vitro* (permeability and cytotoxicity studies in HBMEC and U87 cells) and *in vivo* (pharmacokinetics, tolerability, and efficacy studies). A thorough examination of quality, safety, and efficacy was conducted as part of a comprehensive framework for developing this hybrid nanoplatform, and the findings are detailed in the subsequent sections.

HNP characterization

Colloidal and loading properties of nanoparticles, such as particle size (PS), polydispersity index (PdI), zeta potential (ZP), and drug loading (DL) are summarized in Table 1. The nanoparticles were designed to fit the <100 nm size to better reach the blood–brain barrier and tumor barrier, exploiting the leaky vessels according to the theory of enhanced permeability and retention.[47] The lipid nanoparticles produced had a mean hydrodynamic diameter of 60 nm, narrow distribution, and high stability, see Table 1. However, the addition of stearylamine (usNLCsST), with cationic properties and used as a charge modifier, reverted the negative charge of usNLCs (-37 ± 3 mV to 39 ± 2 mV).

Stearylamine, an amine-containing molecule, was employed to establish a covalent bond with the carboxyl group of aspartic acid in c(RGDfK). The latter served as a linker between lipid and gold nanoparticles.

AuNRs were synthesized by the seedless synthesis method, which yielded CTAB nanorods (AuNRs^{CTAB}) with 24 ± 5 nm × 6 ± 1 nm in size (length × width, with an aspect ratio of 4, see Table 1 and Fig. 1A).[48,49] Morphology analysis of the AuNRs performed by TEM also confirmed their rod shape (Fig. 1A).

Table 1 Particle size (PS), polydispersity index (PdI), zeta potential (ZP), gold content, and celecoxib loading of freshly purified NP formulations. Data are expressed as mean ± SD (n = 3, usNLCs *vs.* other nanoparticles **** $p < 0.0001$)

	PS (nm)	PdI	ZP (mV)	Au content (μg mL^{-1})	Number AuNRs per HNPs (NPs per mL)	DL (%)
usNLCs[b]	59.9 ± 0.3	0.152	−37 ± 3	N.A.	N.A.	4.5 ± 0.1
usNLCsST [b]	64.1 ± 0.2	0.184	39 ± 2****	N.A.	N.A.	4.2 ± 0.1
AuNRs^{CTAB} [a]	N.A.	N.A.	38 ± 2****	37	—	N.A.
AuNRs$^{c(RGDfK)}$ [a]	N.A.	N.A.	−1 ± 1****	32	—	N.A.
HNPs[b]	62.6 ± 1.2	0.134	32 ± 1****	200	1.53×10^3	4.6 ± 0.6
HNPs^{Tf} [b]	60.4 ± 0.1	0.115	29 ± 2****	200	1.53×10^3	4.5 ± 0.3

Stability (1 year)

	PS (nm)	PdI	ZP (mV)
HNPs[b]	67.2 ± 1.2	0.229	39 ± 1
HNPs^{Tf} [b]	76.1 ± 0.5	0.254	29 ± 2

Key: ST – stearylamine; c(RGDfK) – cyclo-(arginine(R)–glycine(G)–aspartic acid(D)–phenylalanine–lysine); Tf – transferrin; HNPs – hybrid nanoparticles; AuNRs – gold nanorods; N.A. – not applicable; Au – gold; DL – drug loading [a] Measured by TEM. [b] Measured by DLS.

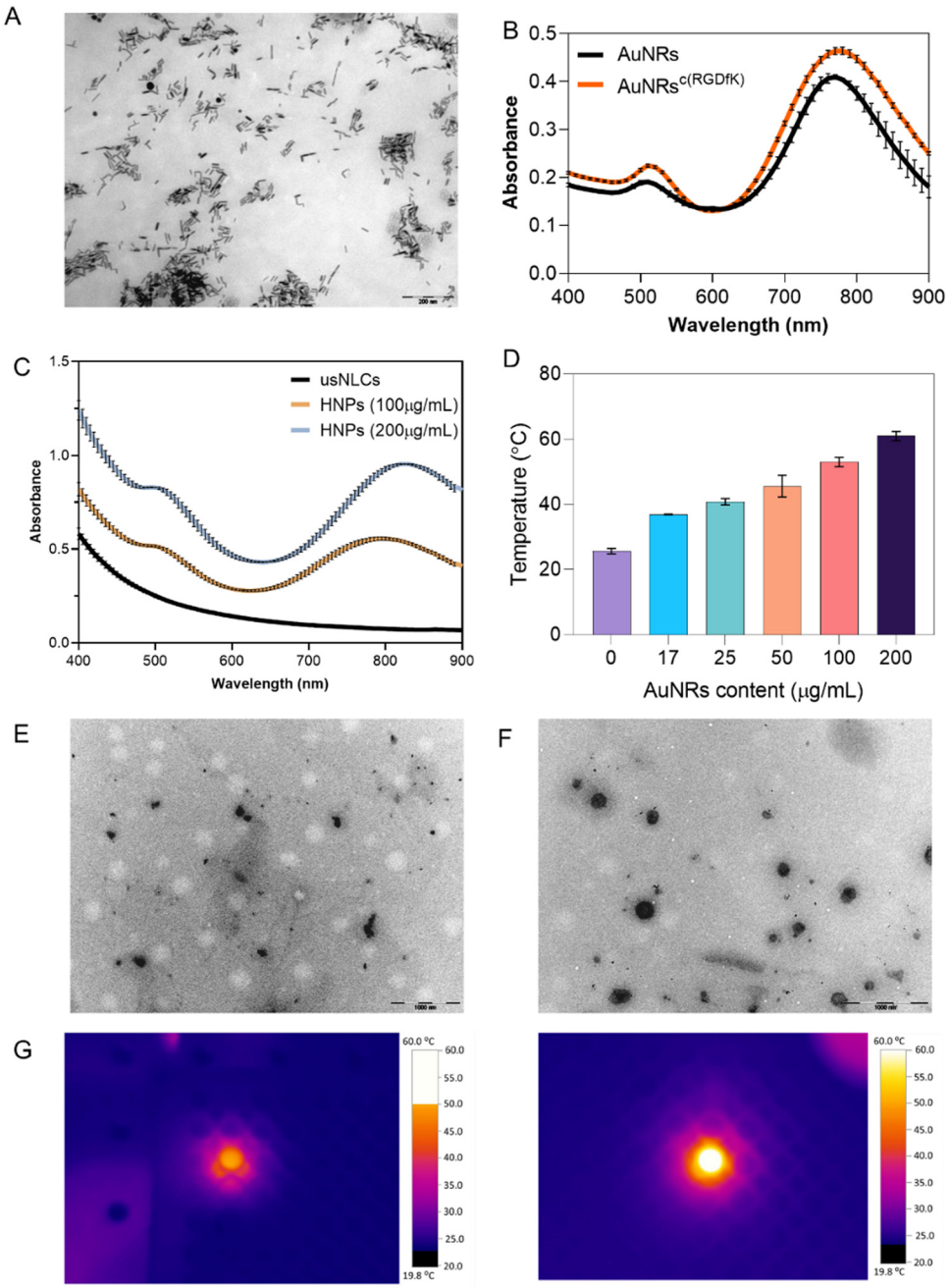

Fig. 1 Nanoparticle characterization. (A) Morphology of AuNRs evaluated by TEM (scale bar = 200 nm). (B) Absorbance spectra of AuNRs and AuNRs$^{c(RGDfK)}$ (black and orange, respectively, n = 5). (C) Absorbance spectra of usNLCsST (black), HNPs$^{Tf(1)}$ (100 μg mL^{-1}, gold), and HNPs$^{Tf(2)}$ (200 μg mL^{-1}, blue) nanoparticles under wavelengths from 400 nm to 900 nm (n = 5). (D) Thermal behavior of HNPs^{Tf} based on the concentration of AuNRs post-NIR laser irradiation (750 nm and light dose of 450 J cm^{-2}). (E) Morphology of HNPs$^{Tf(1)}$ (100 μg mL^{-1}) evaluated by TEM (scale bar = 1000 nm). (F) Morphology of HNPs$^{Tf(2)}$ (200 μg mL^{-1}) evaluated by TEM (scale bar = 1000 nm). (G) Photographs showing the representative colors of HNPs$^{Tf(1)}$ (100 μg mL^{-1}, left) and HNPs$^{Tf(2)}$ (200 μg mL^{-1}, right), reflecting the photothermal conversion effects of NIR laser irradiation (750 nm).

Although CTAB is vital for both the synthesis and stabilization of AuNRs, its use is linked to significant cytotoxicity.[50–54] For this reason, it is important to remove this compound. A prerequisite for the successful functionalization of AuNRs is the existence of functional groups that can establish a stable bond with the metal surface, such as thiol, disulfide, and amine groups.[55–57] Functionalization of the AuNRs was performed by replacing CTAB with the c(RGDfK) peptide through the ligand exchange method. This relies on the strong affinity of gold for the guanidine groups, leading to the shift of CTAB molecules from the AuNRs surface.[58] The ZP of AuNRs changed from positive 38 ± 2 mV to negative −1 ± 1 mV. These changes in ZP indicated successful surface functionalization and corroborated the NMR results. The surface-functionalized c(RGDfK)

showed colloidal stability at 4 °C. As shown in Fig. 1B, the AuNRs displayed a weak peak band at around 520 nm from the transverse plasmon resonance peak band, and the highest longitudinal plasmon resonance peak band around 765 nm demonstrated NIR absorption capability and the potential of photothermal conversion. After being modified with c(RGDfK), the longitudinal resonance absorption peaks of AuNRs exhibited a red shift of 10 nm, *i.e.*, from 750 nm (AuNRs) to 760 nm ($AuNRs^{c(RGDfK)}$), which did not prompt significant changes in the original properties (see Fig. 1B). This shift did not negatively impact the nanoparticle photothermal performance. Note that this behavior has been described in other works wherein a change in the dielectric constant of the surrounding environment of AuNRs was observed.[59–62]

The hybrid nanoparticles were synthesized, as outlined in the ESI.† Colloidal properties showed the conjugation between lipid and gold nanoparticles in accordance with the NMR analysis (Fig. S4–S6 and Tables S1 and S2, ESI†). The addition of $AuNRs^{c(RGDfK)}$ to $usNLCs^{ST}$, establishing the HNPs, previously activated, did not result in any notable change in particle size and polydispersity index ($usNLCs^{ST}$ PS = 64.1 ± 0.2 nm with a PDI = 0.184, HNPs PS = 67.2 ± 1.2 nm with a PDI = 0.134, and $HNPs^{Tf}$ PS = 76.1 ± 0.5 nm with a PDI = 0.115, see Table 1). The TEM images in Fig. 1E and F showed a visual increase in the particle size of HNPs at higher $AuNRs^{c(RGDfK)}$ concentrations. The concentration of AuNRs in the HNP formulation was determined to be 1.53×10^{13} NPs per mL, ensuring a sufficient particle density for subsequent *in vitro* and *in vivo* evaluations. This estimation assumed that the AuNRs have a cylindrical shape ($V = 678.58\ nm^3$) and considering the density of gold ($\rho = 1.93 \times 10^{-20}\ g\ nm^{-3}$). The functionalization of $usNLCs^{ST}$ with $AuNRs^{c(RGDfK)}$ can also contribute to an increase in overall particle size, as the conjugation of AuNRs and the peptide increases the effective hydrodynamic diameter. However, this promoted only a slight change in PS and PDI measured through DLS. Simultaneously, for TEM analysis, the samples were dried as pre-treatment, which might have influenced the aggregation behavior. However, it is important to note that the overall size distribution of HNPs remains relatively narrow, indicating that most particles maintain a consistent size even at higher $AuNRs^{c(RGDfK)}$ concentrations (see Table 1). This suggests that incorporating $AuNRs^{c(RGDfK)}$ into the $usNLCs^{ST}$ is well-controlled and did not significantly affect the overall size distribution. The zeta potential increases in $usNLCs^{ST}$ (compared to usNLCs), and the subsequent addition of $AuNRs^{c(RGDfK)}$ leads to a decrease in the value of this property arising from the formation of a covalent bond between the amine group of stearylamine and the carboxyl group of aspartate residue present in $AuNRs^{c(RGDfK)}$. The HNPs obtained were characterized by UV-vis spectrophotometry, showing that the maximum plasmon resonance peak at 800 nm differed from the maximum peak obtained by $AuNRs^{c(RGDfK)}$ (around 750 nm). This effect can be explained by the increased local refractive index surrounding the $AuNRs^{c(RGDfK)}$ when combined with the $usNLCs^{ST}$ nanoparticles and possible interactions between them. Such red-shifts are commonly observed when AuNRs undergo surface functionalization or aggregation, which could explain the spectral shift with increasing AuNR concentration.[59–62] usNLCs did not display a peak in the spectrum around this wavelength range (Fig. 1C). Note that the CXB assay was not influenced by the addition of AuNRs to lipid nanoparticles, attaining a final drug concentration of ~6.9 mg mL^{-1} for celecoxib.

Stability is a crucial parameter for the practical use of any pharmaceutical formulation. After 1 year, hybrid nanoparticles showed marked stability, with particle size, zeta potential, and drug loading matching the original ranges, see Table 1.

Photothermal conversion

AuNRs and $HNPs^{Tf}$ demonstrated evident photothermal activity through LSPR, exhibiting a response to the 765 nm NIR wavelength. The nanoparticles were exposed to a 750 nm laser and a light dose of 450 J cm^{-2}. Briefly, the AuNRs generated significant heat, reaching an apparent temperature of 70 °C and declining to 37 °C within 3 minutes, whereas the control (usNLCs) did not produce any heat (26.2 °C). $HNPs^{Tf}$ were analyzed according to the amount of AuNRs incorporated (0 μg mL^{-1} to 200 μg mL^{-1}). Fig. 1D presents the changes in the temperature profile of $HNPs^{Tf}$ with an increase up to 60 °C. The highest temperature (at 200 μg mL^{-1}) obtained was near the temperature of neat AuNRs. Consequently, to obtain a better photothermal effect in the subsequent studies, a concentration of 200 μg mL^{-1} AuNRs was added to the usNLCs. These findings suggest that adding lipid nanoparticles and transferrin to the surface of AuNRs does not compromise their capacity to absorb light in the NIR spectrum (as shown previously) and prompts hyperthermia. These results were also confirmed by thermal visualization with an infrared camera (see Fig. 1G).

Cell viability and permeability studies

The cytotoxicity of HNPs and HNP^{Tf} against HBMEC and U87 cells was investigated using the colorimetric resazurin cell viability assay. Overall, a concentration- and time-dependent cytotoxic effect of the nanoparticles on HBMEC and U87 cells was noted within the concentration range of 2.4–2000 μg mL^{-1} for HNPs (considering the lipid content, see Fig. S8A, and B, respectively, ESI†). Also, HNPs are more toxic to HBMEC cells than to U87 cells at 24 h and 72 h (Fig. 2A). Cell viability decreases with an increase in formulation concentration. In HBMEC cells, the IC_{50} values of HNPs and $HNPs^{Tf}$ were calculated after 4 h of incubation, yielding 371 ± 23 μg mL^{-1} and 377 ± 26 μg mL^{-1}, while after 24 h of incubation, the IC_{50} values were 280 ± 21 μg mL^{-1} and 311 ± 10 μg mL^{-1} (Fig. 2A), respectively. These results revealed that the cytotoxicity did not change significantly after surface functionalization for the first 4 h. However, after 24 h, HNPs were slightly more cytotoxic than $HNPs^{Tf}$ (see Fig. 2A). In U87 cells, the IC_{50} values of the HNPs and $HNPs^{Tf}$ were calculated following 24 h and 72 h of incubation. At 24 h, the IC_{50} values of the HNPs and $HNPs^{Tf}$ were 516 ± 62 μg mL^{-1} and 361 ± 84 μg mL^{-1}, while after 72 h of incubation, the IC_{50} values dropped to 250 ± 32 μg mL^{-1} and 124 ± 21 μg mL^{-1} (Fig. 2A), respectively. These results show a higher cytotoxicity for $HNPs^{Tf}$.

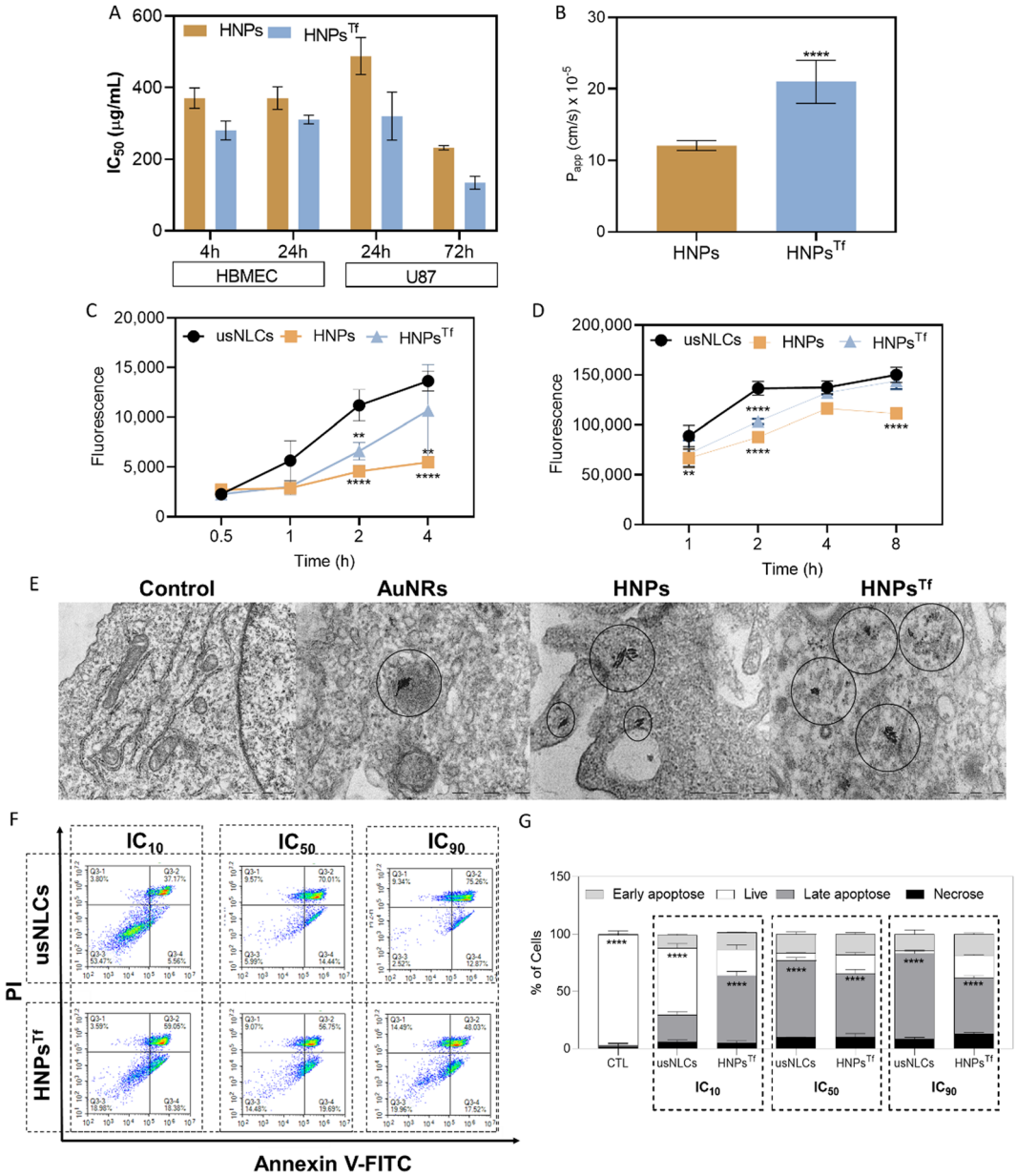

Fig. 2 *In vitro* cellular behavior. (A) IC_{50} values in HBMEC and U87 cells at the indicated times. (B) Apparent permeability coefficient (P_{app}) values in the 2D-model of HBMECs. Data are expressed as mean ± SD (n = 3, usNLCs *vs.* $HNPs^{Tf}$ **** $p < 0.0001$).[63] (C) *In vitro* cellular uptake of celecoxib-loaded usNLCs, celecoxib-loaded HNPs, and celecoxib-loaded $HNPs^{Tf}$ following 0.5, 1, 2, and 4 h of incubation with HBMEC cells. Data are expressed as mean ± SD (n = 9, usNLCs *vs.* HNPs/$HNPs^{Tf}$ ** $p < 0.01$; usNLCs *vs.* HNPs/$HNPs^{Tf}$ **** $p < 0.0001$). (D) Cellular uptake of fluorescent usNLCs, HNPs, and $HNPs^{Tf}$ in U87 cells at 1, 2, 4, and 8 h. Data are expressed as mean ± SD (n = 9). (E) TEM images show the intracellular location of nanoparticles (AuNRs, HNPs, and $HNPs^{Tf}$) in U87 cells after 8 h incubation. (F) The impact on the cell death profile of U87 cells was studied using different concentrations of nanoparticles (IC_{10}, IC_{50}, and IC_{90}). Following 4 h of incubation, cells were stained with Annexin V and propidium iodide (PI), and the percentage of cell death was estimated. Apoptosis assay of U87 cells treated with usNLCs and $HNPs^{Tf}$. Key – Q3.1: necrotic cells, Q3.2: late apoptotic cells, Q3.3: living cells, Q3.4: early apoptotic cells. (G) Relative changes of the percentage in each cell death quadrant. CTL stands for untreated U87 glioblastoma cells. These data are representative of three independent experiments (****$p < 0.0001$).

In addition, the sensitivity of U87 cells to $AuNRs^{c(RGDfK)}$ was evaluated within the range of 0.01–3 μg mL^{-1}, yielding an IC_{50} of 1.1 ± 0.6 μg mL^{-1} at 24 h, see Table S8C (ESI†). The high cytotoxicity of AuNRs compared to hybrid nanoparticles is mainly due to the shape of AuNRs and their particle size (24 ± 5 nm × 6 ± 1 nm in size, length × width, with an aspect ratio of 4, *vs.* 62.6 ± 1.2 nm of $HNPs^{Tf}$). Several studies have shown a size- and shape-dependent cellular toxicity behavior of gold nanoparticles.[64–68]

Overall, the growth inhibitory effect was more pronounced for the hybrid nanoparticles, as compared to usNLCs previously tested, under the same conditions for both cell lines.[63] This can be attributed to the incorporation of AuNRs as an inorganic component in the lipid matrix.

The BBB model was established using Transwell® devices, with cells cultured for 7 days to achieve monolayer formation. BBB integrity was determined by measuring transendothelial electrical resistance (TEER), and the permeability of Lucifer yellow (LY) was assessed at the conclusion of the experiment. TEER values were found within 120–150 Ω cm^2 at the beginning of the experiments.[69] Considering lipid content, celecoxib-loaded HNPs were added to the upper compartment at a concentration of 200 μg mL^{-1}. The IC_{50} values at 4 h were used as a reference to guarantee the integrity of the 2D-BBB model until the end of the experiment. The Pe value of LY below 2.8×10^{-5} cm s^{-1} indicates that there is no adverse effect on the integrity of the cell monolayer, which was checked by the TEER values after 4 h. Fig. 2B shows the effect of celecoxib-loaded HNPs and HNPs^{Tf} on the permeability of celecoxib through the BBB composed of HBMECs in a monolayer. usNLCs were used as a negative control, and usNLCs^{Tf} were used as a positive control, and the results are described in ref. 63. The presence of transferrin on the surface of HNPs (P_{app} = 20.6 $\pm$ 3.42 $\times$ 10^{-5} cm s^{-1} at 4 h) increased the BBB permeability. This can be ascribed to the expression of Tf receptors in HBMECs that enhanced the affinity of HNPs^{Tf} and benefited from receptor-mediated endocytosis. The superior behavior of Tf in the active targeting of usNLCs was previously described in ref. 63. These results are consistent with previous work of our group and other results from the literature.[63,70–74]

Cell uptake and intracellular trafficking

A systematic analysis of cellular internalization was further performed using celecoxib-loaded usNLCs, HNPs, and HNPs^{Tf}. R123 was not covalently bound to nanoparticles. Thus, it was not excluded that R123 was released from the nanoparticles during the cellular uptake. However, it should be noted that the nanoparticles were purified to remove the non-encapsulated R123 before use. Both cells, HBMEC and U87 cells, did not show significant fluorescence on their own, as validated by flow cytometry. Therefore, it is suggested that the fluorescence detected in the cells resulted from the uptake of R123-nanoparticles.

Fig. 2C and D present the mean fluorescence of the cells after incubation with R123-loaded nanoparticles. The results show significant internalization of R123-loaded usNLCs and R123-loaded HNPs over time in HBMEC and U87 cells, respectively. Fig. 2C exhibits high internalization of usNLCs compared to HNPs, being significantly different at 2 h (usNLCs *vs.* HNPs, $p < 0.0001$; usNLCs *vs.* HNPs^{Tf}, $p < 0.005$) and 4 h (usNLCs *vs.* HNPs, $p < 0.0001$; HNPs^{Tf} *vs.* HNPs, $p < 0.005$). Fig. 2D shows higher internalization of usNLCs and HNPs^{Tf} than HNPs, significantly different after 1 h (usNLCs *vs.* HNPs, $p < 0.005$), 2 h (usNLCs *vs.* HNPs, $p < 0.0001$; usNLCs *vs.* HNPs^{Tf}, $p < 0.0001$) and 8 h (usNLCs *vs.* HNPs, $p < 0.0001$; HNPs^{Tf} *vs.* HNPs, $p < 0.0001$). The internalization of nanoparticles was time- and cell type-dependent. Internalization is notably greater in the U87 cells compared to the blood–brain barrier cells (HBMEC), with mean fluorescence 10-fold higher in U87 cells than in HBMECs. Table S3 and S4 (ESI†) shows the effect of surface functionalization (usNLCs/HNPs, usNLCs/HNPs^{Tf}) in HBMEC and U87 cells. The presence of transferrin favored internalization in HBMEC cells (HNPs^{Tf} = 1.2 $\pm$ 0.1 *vs.* HNPs = 1.0 $\pm$ 0.1) at the initial time point. These results were important because the BBB is the first barrier that nanoparticles must overcome to reach the brain tumor. At all the time points, the HNPs^{Tf} values in U87 cells were higher than those of HNPs but lower than those of usNLCs (usNLCs/HNPs^{Tf} < 1).

The internalization of HNPs^{Tf} into cells represents a crucial step for successfully treating glioblastoma through localized photothermal therapy. Cellular TEM images can corroborate the presence of hybrid nanoparticles internalized in the cytoplasm of U87 cells (see Fig. 2E). These findings corroborated the previous cellular uptake data. In turn, fewer AuNRs and HNPs were visualized in U87 cells.

Apoptosis induction

The studies on cell viability revealed that treatment with celecoxib-loaded usNLCs and HNPs^{Tf} induced a significant increase in cell death, indicating that both types of nanoparticles are excellent candidates for effectively eliminating glioblastoma cells. However, the findings on the cell viability did not offer insights into the mechanism of cell death following the treatment.

To elucidate the pathways of cell death induced by the nanoparticles, flow cytometry analyses were conducted to ascertain whether necrosis or apoptosis occurred during the chemotherapy process. Propidium iodide (PI), a non-permeable dye binding to DNA, and Annexin V, which binds to phosphatidylserine, were employed to detect cell death. As caspases initiate apoptotic events, Annexin V migrates to the outer layer of the membrane. This means that viable cells do not bind to Annexin V, whereas cells in early apoptosis can attach to it. Viable cells, or those in the early stages of apoptosis, maintain an intact plasma membrane, PI from passing through. PI stains the nucleus of non-viable cells in the later apoptosis stages, indicating the presence of necrosis and late apoptosis.

To inspect the mechanisms of cell death, U87 cells were treated with three concentrations (IC_{10}, IC_{50}, and IC_{90}) of nanoparticles for 4 h. Annexin V/PI were then applied, and the results are shown in Fig. 2F and G. The main mechanism of cell death was apoptosis, regardless of the concentration used.

In untreated U87 cells, the percentages of total necrosis, early apoptosis, and late apoptosis were 1.97%, 0.79%, and 0.95%, respectively. Cell viability markedly decreased across all experimental conditions treated with usNLCs and HNPs^{Tf}, indicating the effectiveness of nanoparticles in triggering cell death and reducing cell viability, as shown by the results of cytotoxicity studies. The U87 cells died mainly by apoptosis, and a relatively smaller proportion of cells were killed by necrosis after 4 h of treatment with usNLCs and HNPs^{Tf}. Early apoptosis and necrosis were analogous to the concentration studied. Moreover, both nanoparticles induced cell death in a concentration-dependent manner ($p < 0.0001$). At higher concentrations (IC_{50} and IC_{90}), the percentage of late apoptotic cells was higher than for IC_{10}, especially in usNLCs (67.1% and 74.8%, respectively), while for HNPs^{Tf} the apoptotic percentage

was similar at all concentrations tested (58.7, 55.2 and 48.9% for IC_{10}, IC_{50}, and IC_{90}, respectively). The results suggest that hybrid nanoparticles have lower toxicity than lipid nanoparticles at short exposure times (IC_{50} and IC_{90}), especially at high concentrations. These data can be explained by the peptide coating of HNPs, which shows greater protection or lower internalization after 8 h than usNLCs, even at high concentrations (see Fig. 2A). It was also observed that the viability of the cells at the three concentrations decreased significantly compared to the results for untreated cells. This suggests that treatment with these nanoparticles may cause a reduction in cell viability by engaging signaling pathways that control apoptotic outcomes.

A fine-tuning of the performance of the formulations tested was considered (see Fig. S9 and Table S3, ESI†) to reflect a more comprehensive and integrated analysis from an *in vitro* perspective. Accordingly, it is seen that (i) functionalization of usNLCs with c(RGDfK) yields a better cellular internalization, supporting their targeting ability; (ii) the surface modification with Tf assigns an enhanced BBB permeability, justifying their preferential interaction with this physiological barrier; and (iii) the further coupling of usNLCs with AuNRs elicits the best behavior considering cellular viability, uptake, and apparent permeability. This performance grounds the rationale and novelty behind selecting this increasingly complex hybrid nanosystem for subsequent *in vivo* evaluation.

In vivo studies

Hemolysis studies. Hemolysis is characterized by the lysis of the cell membrane of erythrocytes and the release of their content. Evaluation of formulation behavior upon entry into contact with the blood, in particular the hemolytic ability of nanoparticles, is crucial when systemic administration is envisioned. Therefore, the hemolytic behavior of usNLCs, $usNLCs^{ST}$, and $HNPs^{Tf}$ was investigated by *in vitro* incubation with human blood to mimic the possible interaction of the nanoparticles with red blood cells (RBCs). The nanoparticles were tested at different concentrations (1, 10, 50, 100, and 200 μg mL^{-1} considering the lipid content), and the hemolytic activity was evaluated after 3 h of incubation at 37 °C with erythrocytes. None of the formulations induced a percentage of hemolysis exceeding 5%. Triton-X-100 was used as a hemolytic agent, the effect of which can be seen by the red color of the supernatant, while PBS showed no hemolytic outcome. According to the guidelines, only a hemolysis percentage superior to 5% is considered significant.[75] Fig. 3A evidences dose-dependent hemolysis, wherein the formulations exhibit consistent blood compatibility.

In vivo nanoparticle biodistribution analysis

Fluorescence imaging offers a convenient, non-invasive, time- and cost-effective way to detect NPs with the added advantage of requiring a minimal number of animals. The IVIS imaging system, one of the most used methods, offers significant advantages in assessing whole-body biodistribution in live animals or dissected organs.

The biodistribution of the nanoparticles was studied by tracking the fluorescence signal of IR780 using IVIS. IR780, a stable NIR heptamethine dye, was used because of its hydrophobicity. It can be easily loaded into lipid nanoparticles (as usNLCs) and has remarkable properties in NIR fluorescence imaging, avoiding autofluorescence of mouse tissues in IVIS imaging.[76,77] Swiss Nu/+ mice were injected intraperitoneally with $IR780^{free}$, IR780-loaded usNLCs, IR780-loaded HNPs, and IR780-loaded $HNPs^{Tf}$, at a dose of 0.3 mg kg^{-1} (considering the IR780 content). Mice were monitored and kept alive during the testing period. The fluorescence data were normalized considering the fluorescence of the solution and the nanoparticle dispersions, given the different fluorescence intensities. For biodistribution studies, images were collected at different time points. Three animals were sacrificed at 30 h post-injection due to the observed higher accumulation of nanoparticles in the brain. The remaining animals were sacrificed at the last time point of 96 h post-injection. At these time points, the organs were harvested and imaged for fluorescence quantification. The intensity of the NIR fluorescence signals in each organ corresponds to the IR780 accumulation within the organs, as NIR excitation and emission wavelengths typically exhibit low or negligible autofluorescence. Fig. 3B shows the accumulation of nanoparticles in the brain over different time points. The fluorescence signals increased progressively over time, starting with those receiving IR780-loaded usNLCs, followed by IR780-loaded HNPs, IR780-loaded $HNPs^{Tf}$, and finally, those that received $IR780^{free}$.

The fluorescence data obtained with IR780-loaded usNLCs were statistically different compared to the other formulations studied throughout the 96 h timeframe. At 30 h post-injection, all animals exhibited a higher accumulation of IR780 in the brain. The *ex vivo* biodistribution profile in vital organs (brain, heart, liver, kidney, and spleen) were analyzed at 30 and 96 h (Fig. 3C and D, respectively). The fluorescence signals were normalized to organ weight to avoid misinterpretation related to organ size/volume. *In vivo* biodistribution studies presented greater accumulation and retention of usNLCs > $HNPs^{Tf}$ > HNPs > $IR780^{free}$ in the brain at 30 and 96 h (Fig. 3E and F). The NPs' fluorescence intensity in the brain was 2-fold higher at 30 h compared to 96 h. The *ex vivo* images in the brain evidence that usNLCs slowly leave the brain.

Fig. 3C and D show that $IR780^{free}$ and IR780-loaded nanoparticles were mainly accumulated in the kidneys and liver. The higher accumulation in these organs indicates that both serve as elimination pathways. Also, the intensity of usNLC fluorescence in the kidneys and liver was higher compared to $IR780^{free}$ and HNPs/$HNPs^{Tf}$ fluorescence. At 30 h, the accumulation of usNLCs was found to be 2-fold higher than that of the $IR780^{free}$ or NP behavior at 96 h. The preferential accumulation in the kidneys and spleen was reported by other groups that use lipid nanoparticles or hybrid nanoparticles.[78–81] The high intensity observed in the kidneys and spleen reflects the prolonged circulation of these NPs in the bloodstream, attributed to their stealth properties. However, the high accumulation of NPs in the liver highlights the slow clearance of the NPs by the

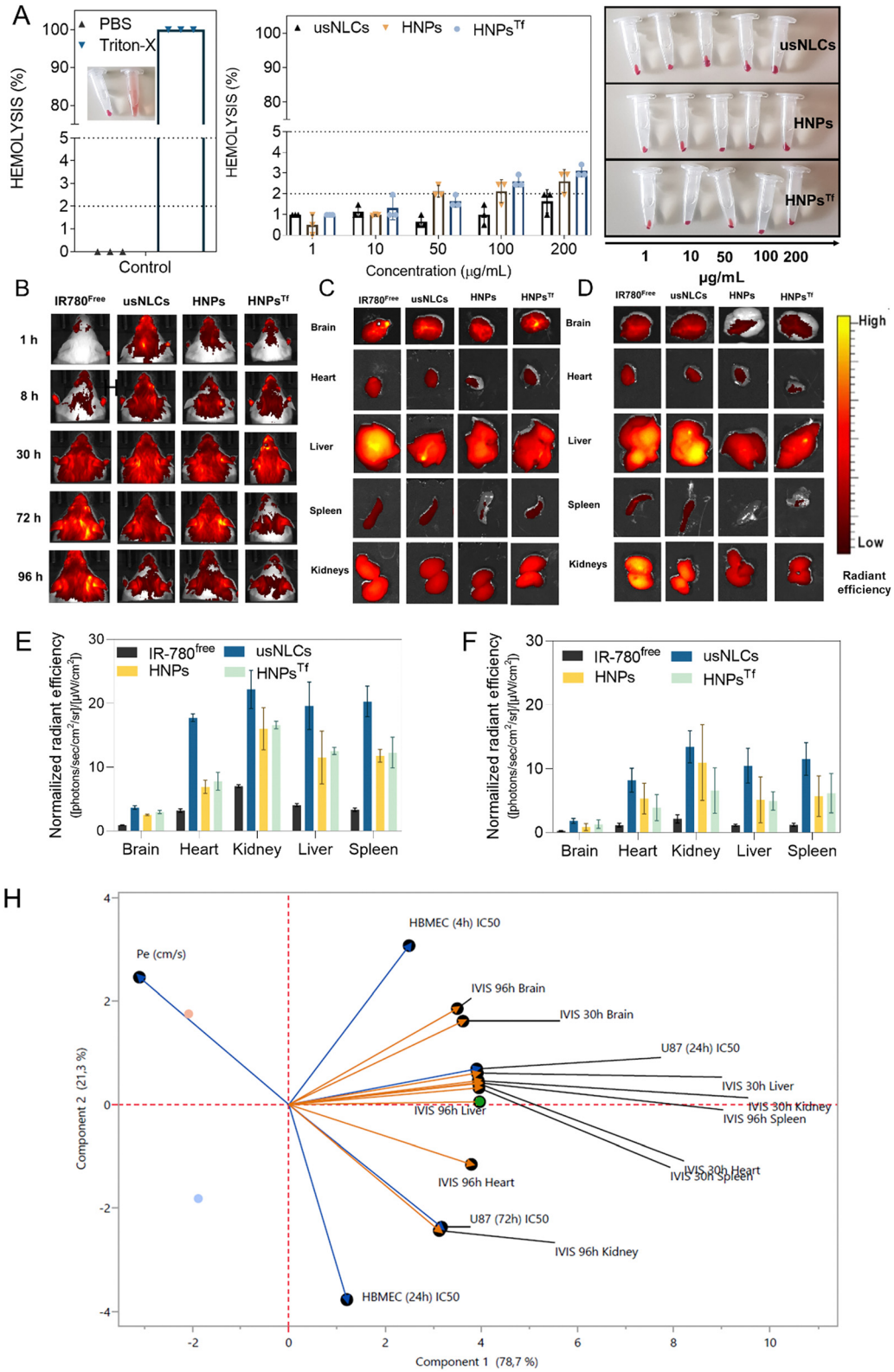

Fig. 3 *In vivo* screening behavior of the nanoparticles. (A) *In vitro* hemolytic activity of usNLCs and hybrid NPs (HNPs and HNPs^{Tf}) in human blood, considering five different concentrations (1, 10, 50, 100, and 200 μg mL^{-1} in relation to lipid content). PBS and Triton-X-100 were used as the negative and positive control, respectively. Results are expressed as mean ± SD, derived from a minimum of three independent experiments conducted with blood samples obtained from distinct donors, each experiment performed in duplicate. (B) *In vivo* fluorescence imaging of IR780 solution and nanoparticles in mice. Fluorescence images of mouse brains acquired at different time points post-injection of IR780-labeled nanoparticles (Ex = 745 nm, Em = 810–875 nm). (C) *Ex vivo* fluorescence images of excised tissues from mice injected with IR780-labeled nanoparticles after 30 h ($2 \leq n \leq 3$) and (D) 96 h ($6 \leq n \leq 7$, Ex = 745 nm, Em = 810–875 nm). (E) Semiquantitative analysis of fluorescence biodistribution in major organs of IR780 solution and nanoparticles at 30 h and 96 h (F) post-injection. Results are presented as mean ± standard deviation. (H) Biplot representation of the three

nanoparticle formulations (usNLCs *vs.* HNPs *vs.* HNPs^{Tf}), the corresponding *in vitro* and *in vivo* performance outcomes on the first two PCs (85.1% and 14.9% of initial information recovery, respectively). The colored points represent the formulations, the blue arrows represent the *in vivo* performance at 30 h (IVIS$_{30h}$ brain, IVIS$_{30h}$ liver, IVIS$_{30h}$ heart, IVIS$_{30h}$ kidney, and IVIS$_{30h}$ spleen), and the orange arrows represent the *in vivo* performance at 96 h (IVIS$_{96h}$ brain, IVIS$_{96h}$ liver, IVIS$_{96h}$ heart, IVIS$_{96h}$ kidney, IVIS$_{96h}$ spleen). Key: IVIS – *in vivo* optical imaging system; P_{app} – permeability apparent coefficient; IC$_{50}$ – half-maximal inhibitory concentration.

reticuloendothelial system.[82] Extended circulation and stealth properties have been identified as advantageous for brain targeting.

Despite the widespread use of fluorescence intensity for biodistribution quantification, there has been a lack of systematic validation of this method across a variety of tissues. Therefore, it is imperative to meticulously assess and interpret fluorescence imaging measurements, as the data may be influenced by tissues with varying degrees of light absorption and scattering. A tissue-specific quantitative comparison is acceptable (*e.g.*, brain *vs.* brain), but it is not correct to determine the accumulated dose by comparing fluorescence intensity between different tissues.

The impact of nanoparticle type on cellular *in vitro* and *in vivo* performance was evaluated using an unsupervised learning algorithm, such as principal component analysis (PCA), using the row-wise estimation method and the correlation matrix. This approach explored similarities, hidden molecular patterns, and differences among distinct nanoparticles, where interactions within the data are not readily visible. This analysis allows for rationalizing preliminary *in vitro* and *in vivo* data. PCA enabled the evaluation of the qualitative effects of nanoparticles on the *in vivo* biodistribution behavior, including the preferential brain targeting and the distribution in off-target organs at two-time points (30 h and 96 h). The interactions are presented in a biplot (see Fig. 3H), which shows the relative positioning of the different nanoparticles (colored points) and the contributions of each variable (colored vectors) on the two principal components (PCs) with an information recovery of 100%. The weight of the vectors indicates how much each variable influences each principal component: a larger magnitude of the vector component upon a principal component signifies a greater impact. The direction of a vector shows the trend and change in the value of the variable. Relevant correlations between variables can also be discerned by examining the angles between vectors: a smaller angle indicates a stronger correlation.

The nanoparticles are distributed across three quadrants: regarding the usNLCs, they are the mostly impacted by the analyzed variables. The *in vitro* performance of usNLCs in U87 cells showed a higher IC$_{50}$, indicating a lower capacity to promote cell death. Their *in vivo* behavior indicates a higher accumulation in off-target organs, along with a higher accumulation in the brain. Conversely, HNPs^{Tf} demonstrated a higher cytotoxic effect in U87 cells and the best permeability through the blood–brain barrier, primarily ascribed to the presence of Tf, which actively targets the transferrin receptor described in HBMECs. In terms of *in vivo* behavior, HNPs^{Tf} display lower brain biodistribution compared to usNLCs but showed reduced accumulation in off-target organs. HNPs exhibited generally decreased *in vitro* and *in vivo* performance compared to usNLCs and HNPs^{Tf}. A comprehensive analysis of *in vitro* and *in vivo* performance enabled the selection of the usNLCs and HNPs^{Tf} formulations for further *in vivo* studies.

In vivo pharmacokinetic parameters

The *in vivo* studies also aimed to characterize and understand the pharmacokinetics of celecoxib after intraperitoneal (i.p.) administration of usNLC, usNLC$^{c(RGDfK)Tf}$, HNP, and HNP^{Tf} formulations, as compared to a control group receiving the non-encapsulated drug at the same dose (20 mg kg^{-1}). The pharmacokinetic profiles of celecoxib concentration in plasma, brain, liver, spleen, and kidney are displayed in Fig. S10 (ESI†), respectively. Non-compartmental analysis was carried out to obtain various pharmacokinetic parameters,[83] which are summarized in Table 2. The following subsections describe the behavior throughout the different matrices.

Plasma pharmacokinetic profiles. As previously reported by our group,[84] the C_{max} of i.p. administered celecoxib in solution was 9.10 μg mL^{-1} after 1 h (t_{max} value), considering the plasma. In contrast, the encapsulation of celecoxib in usNLCs, usNLCs$^{c(RGDfK)Tf}$, HNPs, and HNPs^{Tf} showed an improvement, with a C_{max} of 10.6 μg mL^{-1}, 22.0 μg mL^{-1}, 7.0 μg mL^{-1}, and 8.8 μg mL^{-1} after 0.5 h, respectively. The magnitude of celecoxib absorption from lipid nanoparticles and hybrid nanoparticles, expressed by AUC$_{0\text{-last}}$, was significantly higher for usNLCs (85.4 h × μg mL^{-1}) in comparison to other nanoparticles (usNLCs$^{c(RGDfK)Tf}$, HNPs and HNPs^{Tf}, 48.0 h × μg mL^{-1} *vs.* 27.5 h × μg mL^{-1} *vs.* 45.6 h × μg mL^{-1}, respectively) and celecoxib in solution (40.2 h × μg mL^{-1}).

Brain distribution. Celecoxib encapsulated in nanoparticles reached the brain faster (0.5 h) than celecoxib in solution and usNLCs$^{c(RGDfK)Tf}$ (1 h). Taking into consideration the AUC$_{0\text{-last}}$ in the brain, a higher amount of celecoxib was prompted by usNLCs (64.3 h × μg mL^{-1}, 6.24 times higher than the usNLCs^{cRGDfKTf}) followed by HNPs^{Tf} (39.8 h × μg mL^{-1}, 2.24 times higher than the HNPs). Also, the usNLCs exhibited a higher blood–brain barrier celecoxib crossability, followed by HNPs^{Tf}. Although C_{max} in the brain is a relevant parameter as it indicates the peak drug concentration in the organ following administration, the AUC$_{0\text{-last}}$ reflects the drug's overall therapeutic effect. Despite the similar C_{max} values between formulations (HNPs 5.6 h × μg mL^{-1} *vs.* HNPs^{Tf} 5.1 h × μg mL^{-1}), the AUC$_{0\text{-last}}$ of HNPs^{Tf} is 2.24-fold higher compared to HNPs, highlighting its superior drug exposure over time. This enhanced pharmacokinetic profile supports the selection of usNLCs and HNPs^{Tf} for efficacy studies in GB, as sustained drug availability in the brain is crucial for therapeutic success. Note that $t_{1/2}$ and MRT (mean residence time) are higher in the plasma and brain when the drug is encapsulated. These positive

Table 2 Pharmacokinetic (PK) parameters for celecoxib in nanoparticle formulations were evaluated relative to the free drug in solution across the plasma, brain, liver, spleen, and kidney[83]

	Celecoxib (CXB)[a]					CXB-usNLCs					CXB-usNLCs$^{c(RGDfK)Tf}$				
PK parameters	P	B	S	K	L	P	B	S	K	L	P	B	S	K	L
$t_{1/2}$ (h)	3.3	4.5	3.8	4.0	3.2	10.9	9.7	85.6	13	3.2	13.4	9.4	9.6	—	3.5
t_{max} (h)	1	1	1	1	0.5	0.5	0.5	0.5	0.5	0.5	0.5	1	0.5	0.5	0.5
C_{max} (μg mL^{-1} or μg g^{-1})	9.1	20.6	22.4	15.6	10.6	10.6	12.8	21.1	19.8	30.6	22.0	3.2	1.4	15.6	37.3
$AUC_{0\text{-last}}$ (h × μg mL^{-1} or h × μg g^{-1})	40.2#	50.2#	156.7#	57.9#	55.2#	85.4	64.3	178.7	50.4	97.8	48.0#	10.9#	3.2	20.0#	65.4#
AUC_{inf} (h × μg mL^{-1} or h × μg g^{-1})	40.3#	50.5#	157.5#	58.2#	55.3#	103.8	70.4	918.6	59.9	97.9	50.9#	11.6#	3.5	—	65.6#
AUC_{extrap} (%)	0.3	0.6	0.5	0.5	0.2	17.7	8.7	80.5[b]	15.8	0.1	5.7	5.8	9.4	—	0.2
MRT (h)	3.7	3.3	4.8	3.9	4.3	15.3	11.9	126.9	15.7	4.5	5.6	8.7	11.0	—	2.7

	CXB-HNPs					CXB-HNPs^{Tf}				
PK parameters	P	B	S	K	L	P	B	S	K	L
$t_{1/2}$ (h)	11.5	13.3	5.7	—	—	7.5	10.7	9.4	—	—
t_{max} (h)	0.5	0.5	0.5	0.5	0.5	0.5	0.5	1	3	1
C_{max} (μg mL^{-1} or μg g^{-1})	7.0	5.6	18.7	7.4	43.9	8.8	5.1	15.6	6.6	18.3
$AUC_{0\text{-last}}$ (h × μg mL^{-1} or h × μg g^{-1})	27.5	17.4	162.4#	15.0#	105.7#	45.6	39.8	139.1	27.0#	43.3#
AUC_{inf} (h × μg mL^{-1} or h × μg g^{-1})	31.7	21.2	163.6#	—	—	49.1	45.3	156.4	—	—
AUC_{extrap} (%)	13.1	17.9	0.8	—	—	7.2	12.0	11.0	—	—
MRT (h)	13.1	15.1	9.7	—	—	10.3	13.2	12.9	—	—

Key – P, plasma; B, brain; L, liver; S, spleen; K, kidney; t_{max} – time to reach maximum concentration; C_{max} – maximum concentration; $AUC_{0\text{-inf}}$ – area under the concentration time-curve from time zero to infinite; $AUC_{0\text{-last}}$ – area under the concentration time-curve from time zero to the previous measurable drug concentration; MRT – mean residence time. For the estimation of pharmacokinetic parameters, time points with concentrations below the limit of quantification (LoQ) were assigned a value of half the LoQ (#). [a] Data published in ref. 84 and reused with permission. [b] Extrapolated area >20% of the total.

findings can be attributed to the small particle size and their lipophilic characteristics, along with a high CXB loading capacity. Together, these factors are possible to contribute to improving the permeability of the nanoparticles across the membrane.

Off-target organ distribution. To evaluate the biodistribution of celecoxib in solution and encapsulated in nanoparticles, two parameters were considered: the DSI and the DTI. As previously mentioned, DSI is the ratio used to measure the drug content in each organ compared to plasma, with DSI values above 1 indicating higher selectivity for that organ. DTI is the ratio used to quantify the proportion of drug content present in a specific organ following the administration of encapsulated and non-encapsulated formulations. It is important to highlight that this analysis prioritized a comprehensive biodistribution evaluation across various matrices. Fig. 4 displays the DSI and DTI ratios. Despite reaching the brain later, celecoxib in solution had a higher DSI (1.20), as previously reported,[84] whereas the usNLC, usNLC$^{c(RGDfK)Tf}$, HNP and HNP^{Tf} values were 0.75, 0.23, 0.63 and 0.87, respectively. Moreover, celecoxib in solution showed a similar behavior or higher DSI values than the nanoparticles in off-target organs, such as the liver, kidney, and spleen (see Fig. 4).[84] The results evidenced high accumulation in the spleen, followed by the liver and kidney, which is different from the IVIS biodistribution, where the higher clearance occurred essentially in the liver and kidneys. DTI values illustrated the brain-targeting effect of celecoxib prompted by usNLCs with a DTI exceeding 1, while HNPs^{Tf} exhibited a DTI of 0.79, followed by HNPs (0.34) and usNLCs$^{c(RGDfK)Tf}$ (0.21), see Fig. 4. In contrast, high DTI values were obtained for usNLCs in the spleen (1.14) and HNPs (1.03), while for HNPs^{Tf}, 0.89 was found, and usNLCs$^{c(RGDfK)Tf}$ had a value of 0.02, highlighting the sparing effect in this off-target organ induced by the NP functionalization. A similar behavior was observed for liver with HNP^{Tf} displaying 2.25 times less accumulation in this organ in comparison to usNLCs (see Fig. 4). The reduced hepatic uptake observed when nanoparticles are functionalized with Tf can be attributed to several factors, including competition with endogenous transferrin in the liver, as it is the major organ that produces transferrin, and a higher expression of TfR1 in U87 cells.[85–87] These mechanisms both contribute to enhance the accumulation of functionalized nanoparticles at the brain/tumor site while minimizing hepatic accumulation, which can be demonstrated by the results presented in the DTI values from targeting nanoparticles (see Fig. 4, usNLCs$^{c(RGDfK)Tf}$ and HNP^{Tf}).

In sum, usNLCs seem to exhibit a preferential targeting towards the brain while being eliminated more rapidly by clearance organs. Note, however, that DTI values below 1 in HNPs^{Tf} indicate a decreased accumulation in the off-target organs.

Anti-tumor efficacy

Repurposed drug effect. An orthotopic U87 glioblastoma model in Swiss nude mice was further used to evaluate (i) the efficacy of celecoxib as a repurposed anticancer drug, (ii) the benefit of encapsulation of celecoxib in lipid nanoparticles, and (iii) the efficacy of a hybrid system, compared with the standard drug, temozolomide.

Prior to the initiation of tumor treatment, different concentrations of free drugs (celecoxib and temozolomide) were tested to evaluate the animal tolerability during the treatment regimen. The selected treatment regimen required two cycles of five

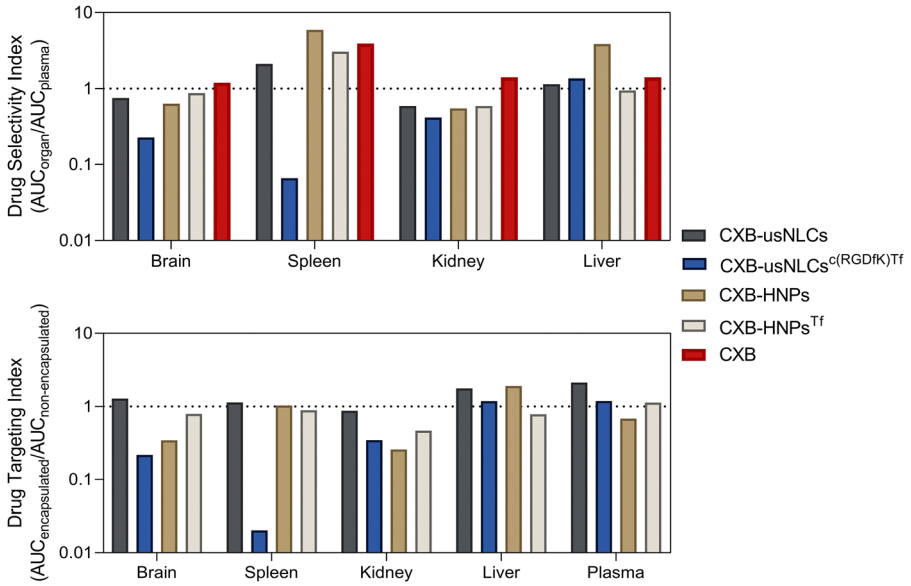

Fig. 4 Drug selectivity indices (DSI) and drug targeting indices (DTI) for CXB in the brain, liver, spleen, and kidney were estimated using mean AUC data. A DSI higher than 1 indicates a preference for drug selectivity towards the corresponding matrix, whereas a DTI greater than 1 suggests a preference for targeting the encapsulated drug to the respective organ.[83] The free CXB data have been previously published in ref. 84. Its inclusion is essential for a comprehensive understanding of the results. Data were reused with permission.

consecutive administrations, and the celecoxib in solution exhibited toxicity at doses higher than 5 mg kg^{-1}. In contrast, the encapsulation of celecoxib in nanoparticles allowed a dose four times higher (20 mg kg^{-1}). Animals were then randomly divided into six treatment groups: saline, celecoxib in solution, temozolomide in solution, celecoxib-loaded usNLCs, and celecoxib-loaded $HNPs^{Tf}$. Note that the standard treatment started 21 days after U87 cell implantation. Importantly, mice treated with free drugs showed little change in body weight (see Fig. S11, ESI†), indicating that both drugs had mild systemic toxicity; however, the two-day break made it possible to recover and gain weight at the end of the two cycles (Fig. S11, ESI†). Note that this study considered a comparison among the better-performing nanoparticle formulations, *i.e.*, usNLCs and $HNPs^{Tf}$, grounded on the well-established efficacy parameters outlined in our previous studies,[32] and to achieve statistically significant outcomes with the fewest animals necessary (3R ethical principles).

Quantitative analysis of tumor growth over time is represented in Fig. 5A, estimated by MRI. It shows a tumor growth suppressing effect by lipid nanoparticles (celecoxib-loaded usNLCs), hybrid nanoparticles (celecoxib-loaded $HNPs^{Tf}$), and temozolomide in solution, compared with both saline and celecoxib solution. Tumor growth was more pronounced in the control group during the 21^{st} and 34^{th} days, corresponding to the treatment period. Celecoxib solution and celecoxib-loaded usNLCs inhibited the growth of glioblastoma cells, but the effect was not significant; the mice were mainly sacrificed at 48 and 51 days after the tumor implantation, see Fig. 5B. The control group behavior and free celecoxib were similar, meaning that the amount of free celecoxib was not sufficient to treat the tumors. In addition, celecoxib-loaded $HNPs^{Tf}$ groups exhibited a therapeutic effect on glioblastoma tumors. The therapeutic performance of celecoxib-loaded $HNPs^{Tf}$ showed a significant result in 1 animal that survived to day 84 after tumor implantation, see Fig. 5B. These results suggest that celecoxib-loaded $HNPs^{Tf}$ could not prevent the tumor progression (Fig. 5A). Temozolomide in solution was administered orally, in which only one animal survived, without tumor recurrence. The mean survival time (MST) of the $HNPs^{Tf}$ was 55 days, indicating a better anti-glioblastoma effect compared to the control group (43 days), followed by celecoxib in solution (48 days), and celecoxib-loaded usNLCs (51 days), see Table 3. These results indicate that $HNPs^{Tf}$ exhibited a higher efficacy, in relation to celecoxib free and loaded usNLC as substantiated in the section "*In vivo* pharmacokinetics parameters". These outcomes are consistent with the *in vitro* studies, indicating a higher cytotoxicity of $HNPs^{Tf}$ than of usNLCs in U87 cells.

MRI serves as a direct observation of brain areas, and in the present study, it was employed to examine tumor progression weekly up to 91° days after cell inoculation (Fig. 5C). HNP^{Tf}-treated mice exhibited a prolonged life-time, when compared with those of other groups (control, celecoxib, celecoxib-loaded usNLCs, and temozolomide). As mentioned earlier, the tumors evidenced no differences in growth among groups during the treatment days, except in the control group. However, two weeks after the end of treatment, the tumor exhibited exponential growth (see Fig. 5A and B).

For this study, two hypotheses were set forth: first, whether celecoxib could treat glioblastoma, and second, whether there is a synergistic effect between celecoxib and photothermal therapy to treat glioblastoma. Celecoxib achieved better results than the control group, and when encapsulated, it still had better efficacy than celecoxib in solution and the drug described as first-line treatment (temozolomide).

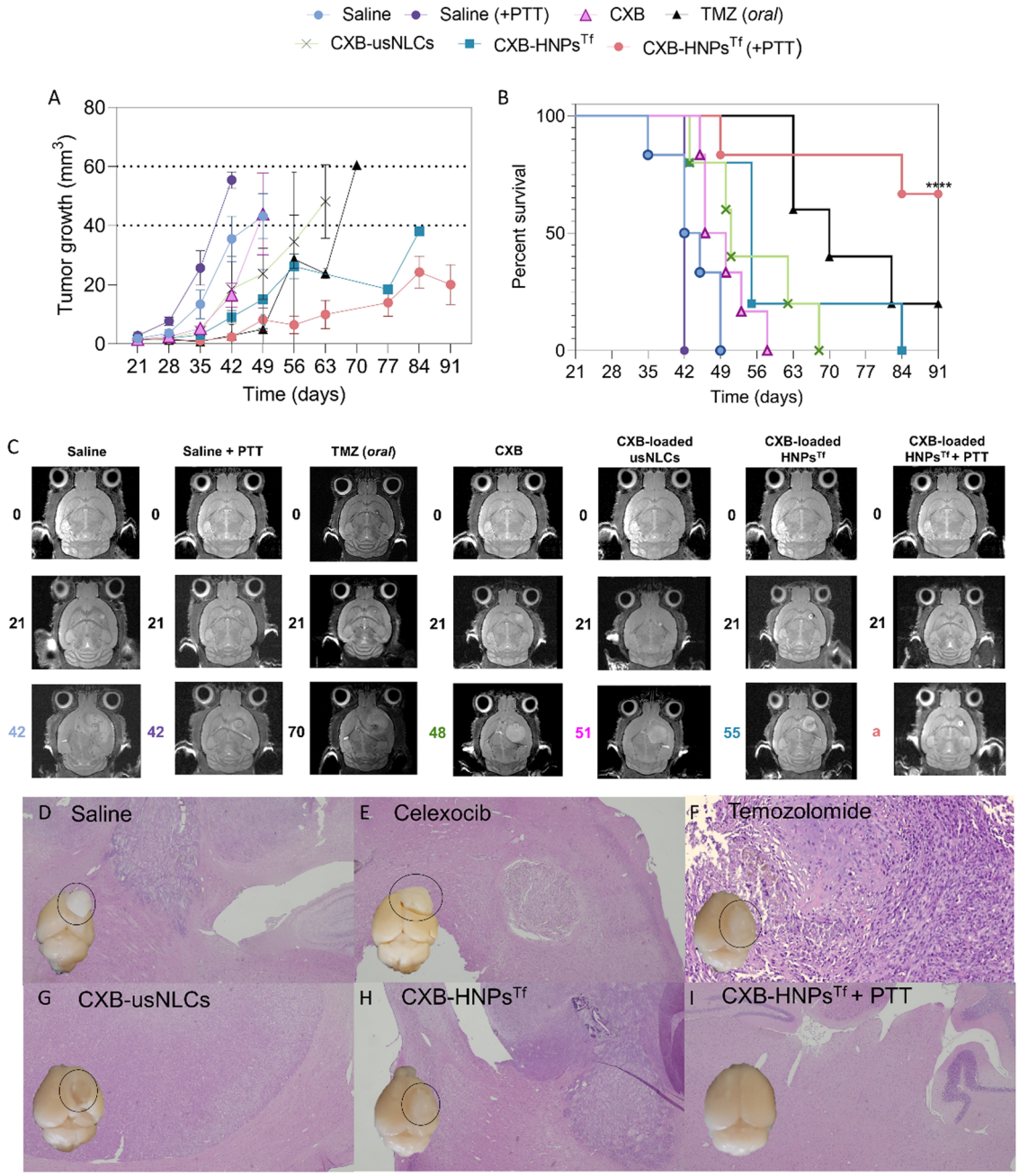

Fig. 5 *In vivo* anti-tumor efficacy of nanoparticles evaluated using an orthotopic Swiss nude mouse model. (A) Representation of the tumor growth of the control (0.9% NaCl), free drugs (temozolomide and celecoxib), and nanoparticles (usNLCs, HNPs^{Tf}, and HNPs^{Tf} + photothermal therapy). (B) Kaplan–Meier survival curves of animals administered with free drugs *vs.* nanoparticles. **** $p < 0.0001$ by Mantel–Cox test. Data presented as mean ± SD (n = 6). (C) Tumor growth monitoring. Representative MR imaging measurements of glioblastoma-bearing mice (21, 42, 49, 56, 70, and 91 days) analysis of a coronal section view. Haematoxylin and eosin staining revealed an implanted glioblastoma tumor and the distinct boundary between glioblastoma cancerous tissue and normal tissue with preserved morphology (a = undefined survival time). Saline group (D), celecoxib group (E), temozolomide group (F), celecoxib-loaded usNLCs (G), celecoxib-loaded HNPs^{Tf} (H), and celecoxib-loaded HNPs^{Tf} (+ irradiation, I).

Chemo- and photothermal effects. To inspect the photothermal therapeutic effects of HNPs^{Tf} in terms of antitumor efficacy, an orthotopic U87 glioblastoma model was again established in Swiss nude mice, and the tumor volume was evaluated every 7 days by MRI. The treatment started 21 days after U87 cell implantation. Nanoparticles were i.p. administrated, and we aimed to demonstrate whether the HNPs^{Tf} can be used as a potential nanoparticle for chemo/photothermal therapy *in vivo*. The administered dose was previously established (celecoxib = 20 mg kg^{-1}). To ensure a sufficient amount of AuNRs in the brain at the irradiation time and, consequently, the photothermal effect, an additional volume (200 μL) of unloaded HNPs^{Tf} was administered. This strategy ensures the photothermal effect since the Au concentrations in the brain must exceed

Table 3 *In vivo* outcomes, including the median survival time, survivals at certain time points, tumor-growth delay, percentage of tumor volume growth, and percentage of tumor volume growth inhibition (data represented as mean ± SD, $3 \leq n \leq 6$)

Treatment group	MS	S56	S91	% TGD	% TGI42	% TGI
Saline[b]	44	0/6	0/6	N.A.	N.A.	N.A.
Saline + PTT[c]	42	0/3	0/3	N.A.	N.A.	N.A.
TMZ (*oral*)	70	5/5	1/5	54 ± 11	95 ± 3	42 ± 14
CXB	48	1/6	0/6	15 ± 5	63 ± 6	13 ± 6
CXB-usNLCs	51	2/5	0/5	29 ± 7	85 ± 2	15 ± 6
CXB-HNPs^{Tf}	55	1/5	0/5	38 ± 12	91 ± 2	38 ± 12
CXB-HNPs^{Tf} + PTT	[a]	5/6	4/6	85 ± 10[b]	98 ± 1[b]	71 ± 13[b]
				103 ± 10[c]	98 ± 1[c]	78 ± 10[c]

N.A. – not applicable. Key: MS – median survival (days); S56 – survivals at 56 days; S91 – survivals at 91 days; TGD – tumor growth delay; TGI – tumor growth at the threshold; TG – tumor growth at 42 days. [a] Undefined. [b] Data compared with the saline group. [c] Data compared with the saline + PTT group.

20 μg mL^{-1}. As studied in the section "photothermal conversion", the photothermal conversion depends on the AuNR concentration. Animals were randomly assigned to the two treatment arms: saline plus NIR irradiation and HNPs^{Tf} plus NIR irradiation. The treatment regimen was the same as mentioned above (5 consecutive days, 2 days off, and another 5 consecutive days), and the animals were irradiated every 6 h after administration.

As shown in Fig. 5A, tumors in the saline (+ PTT) group grew up to 40 mm^3 within 42 days (20-fold in volume since the start of treatment). This result shows that the laser does not affect tumor growth. Tumor volume in the celecoxib-loaded HNPs^{Tf} (+ PTT) irradiation group grew to 10 mm^3, which is 8 times the volume since the start of laser treatment. Celecoxib-loaded HNPs^{Tf} (+ PTT) slowed tumor growth with a 4.10-fold inhibition of tumor volume from day 21 (first day of treatment), which is considered statistically different compared with the saline group. Importantly, these results suggest that the single treatment with celecoxib-loaded HNPs^{Tf} was not enough to eliminate the tumors (MS HNPs^{Tf} = 55 days); however, the group treated with celecoxib-loaded HNPs^{Tf} + PTT exhibited an efficient tumor growth inhibition during the 91 days post-treatment start, see Fig. 5A and B.

To understand the impact of different treatments, tumor growth delay (TGD) and tumor growth inhibition (TGI) were used to assess the effects of treatments on tumor progression (Table 3). The mean survival time of the celecoxib-loaded HNPs^{Tf} + PTT group was 91 days, and the antitumor effect was remarkably higher (98% growth delay and 78% inhibition growth compared to the corresponding saline group), see Table 3. The tumors treated with celecoxib-loaded HNPs^{Tf} + PTT exhibited a higher percentage of TGD than temozolomide, with 85% and 54% growth delays, respectively. Concerning TGI, the results demonstrate the effect of encapsulation of CXB, which allowed administration of a higher dose (5 mg kg^{-1} CXB in solution *vs.* 20 mg kg^{-1} CXB encapsulated) and confirms that tumor size did not increase during the administration period (TGI42 was similar in all groups except for CXB in solution). Also, laser-irradiated HNPs^{Tf} prompted a tumor inhibition efficiency that was 1.86 times higher than temozolomide, with a TGI of 78% compared to 42%. This result provides proof of concept that celecoxib-loaded HNPs^{Tf} can accumulate and effectively release celecoxib into the brain by NIR irradiation, leading to effective inhibition of tumor growth (Fig. 5D).

It should be noted that in brain tumors, the poor drug penetration caused by the blood–brain barrier and blood-tumor barrier leads to a lower therapeutic efficacy. The presence of targeting molecules (Tf and c[RGDfK] for the BBB and BTB) could facilitate the passage of nanoparticles through the BBB as well as selective uptake by glioblastoma cells. Cellular studies have already confirmed these results (permeability through HBMECs and cellular uptake in U87 cells). Moreover, chemo- and photothermal therapy synergistically contributed to the anti-glioblastoma effect of HNPs^{Tf}, which can be attributed to the NIR-triggered brain accumulation of the drugs and glioblastoma targeting. Chemo- and photothermal therapy reduced the local recurrence and demonstrated the ability to prolong the survival rate in this animal model. Throughout the treatment process, the weight of the mice remained stable, with some changes during the 12 days of administration, but all animals regained weight by the end of the study.

Although therapeutic efficacy in mice is promising, translating these results to clinical settings, particularly envisioning the NIR propagation through the human skull, presents significant challenges. However, this task may be feasible resorting to several strategies.[88–91] One of them concerns the laser interstitial thermal therapy (LITT), which offers a less invasive alternative to traditional brain surgery. This technique involves implanting a laser catheter into the tumor and heating it to temperatures high enough to ablate the tumor cells. Another promising strategy is magnetic fluid hyperthermia (MFH). An example of the MFH implementation is the already approved Nanotherm®, a colloidal suspension of amino silane coated with iron oxide nanoparticles able to generate heat in the presence of a magnetic field, therefore effectively destroying glioma cells.[92]

Despite these promising alternatives, it is crucial to evaluate the potential risks and benefits of each medical procedure on a case-by-case basis.

Histological outcomes. Evaluation of the cross-section of GB tumor tissue stained by the haematoxylin and eosin method showed that tumor morphology differed among the tested groups (see Fig. 5D–I). The saline group (with or without irradiation) and the celecoxib solution group exhibited similar behavior, with an expansively growing solid tumor lesion and microvascular proliferation (see Fig. 5D and E). Comparing the efficacy of anticancer properties of celecoxib-loaded usNLCs with those of celecoxib-loaded HNPs^{Tf}, after the celecoxib-loaded usNLCs treatment the morphology of tumor tissue displayed an increased proliferation index, high density of cells, and mild necrosis (5%), whereas the celecoxib-loaded HNPs^{Tf} group showed 50% necrosis and some calcification areas (see Fig. 5F and G). The temozolomide group showed calcification areas. The best result was obtained for the celecoxib-loaded HNPs^{Tf} (+ irradiation) without signs of brain changes (see Fig. 5H and I). This evidence

supports the superior performance of celecoxib-loaded HNPs^{Tf} (+ irradiation) in tumor regression.

Biochemical analysis. The animal groups were tested for potential toxicity and checked if treatments could affect both liver and kidney functions (Fig. S12, ESI†). Blood samples were collected *via* cardiac puncture. Normal levels of biomarkers were determined in the serum samples of the saline groups. None of the biomarker (AST, ALT, ALP, GGT, CK, and U) levels indicated statistical differences with those of the saline solution, nanoparticles, or nanoparticles plus irradiation groups. However, administration of drugs in solution resulted in an increase in CK and AST levels. CK is an indicator of cardiotoxicity, and CK values were 1.32-fold (temozolomide) and 1.17-fold (celecoxib) higher than the saline group after the treatment with free drugs, whereas no increase was observed after treatment with nanoparticles. Cardiotoxicity is a known side effect of temozolomide.[93] Additionally, the biomarker values for mice administered with HNPs^{Tf} (with or without NIR irradiation) were similar to saline groups (with or without NIR irradiation). No significant changes in serum GGT levels were detected.

This *in vivo* biochemical analysis of serum samples suggests mild cardiotoxicity of temozolomide and celecoxib. However, the drug encapsulation (such as celecoxib) in nanoparticles has the potential to reduce the severity of conventional chemotherapeutics in the clinic that are known to cause adverse effects. These outcomes suggest that the celecoxib-loaded HNPs^{Tf} demonstrate a promising synergistic chemo/photothermal effect along with great biocompatibility, warranting further *in vivo* studies and potential clinical translation to treat glioblastoma patients.

Conclusions

In summary, targeted hybrid nanoparticles were developed to confirm the feasibility of delivering both the chemotherapeutic drug and photothermal therapy simultaneously to the tumor region. This approach aims to exert a synergistic effect for glioblastoma treatment. The surface of the hybrid nanoparticles was functionalized with transferrin, a blood–brain barrier targeting agent, and the covalent binding between two types of nanoparticles (usNLCs and AuNRs) was performed by c(RGDfK) peptide, which is also known to be a specific target for glioblastoma cells.

The celecoxib-loaded HNPs^{Tf} were found to promote a noteworthy anti-glioblastoma targeting effect. The hybrid nanoparticles were easily synthesized, with a well-defined structure and size, excellent photothermal behavior, and a biocompatible nature. The *in vitro* studies on HBMEC showed effective permeabilization and a consequent accumulation and retention in glioblastoma cells (U87 cells). The targeting ability to HBMECs is explained by the presence of transferrin, which is easily recognized by the Tf-mediated receptor, broadly expressed in the blood–brain barrier and in glioblastoma cells. The *in vivo* results were consistent with the *in vitro* outcomes, and showed chemo-photothermal abilities of hybrid nanoparticles, leading to a synergistic anticancer effect. The low toxicity of celecoxib-loaded HNPs^{Tf} at high dose was demonstrated in mice by histological and biochemical analysis.

In conclusion, the development of celecoxib-loaded HNPs^{Tf} represents an adaptable strategy for creating targeted nanoparticles that combine the desired synergistic therapeutic functionalities for glioblastoma. Apart from photothermal therapy, given the photoacoustic imaging capability of gold nanorods (not explored in the current work), they also open new avenues for the potential application of celecoxib-loaded HNPs^{Tf} for theranostic purposes.

Author contributions

Maria Mendes (conceptualization: lead; data curation: lead; formal analysis: equal; writing – original draft: lead). Maria António (investigation: supporting; methodology: supporting). Ana L. Daniel-da-Silva (investigation: supporting; writing – review & editing: supporting). Rui Oliveira (investigation: supporting; methodology: supporting). Luís G. Arnaut (resources: supporting; writing – review & editing: supporting). Célia Gomes (resources: supporting; writing – review & editing: supporting). Maria L. Ramos (data curation: equal; formal analysis: equal; writing – review & editing: supporting). José Sereno (data curation: supporting; formal analysis: supporting; investigation: supporting; methodology: supporting). Miguel Castelo-Branco (investigation: supporting; methodology: supporting). João J. Sousa (resources: supporting; supervision: supporting). Alberto Pais (resources: supporting; supervision: supporting; writing – review & editing: supporting). Carla Vitorino (conceptualization: lead; data curation: supporting; supervision: lead; writing – review & editing: lead).

Data availability

Data will made available upon request to the author.

Conflicts of interest

There are no conflicts to declare.

Acknowledgements

Fundação para a Ciência e a Tecnologia (FCT) supports the Coimbra Chemistry Centre through the Project UID/QUI/00313/2020. Maria Mendes acknowledges the PhD research grant SFRH/BD/133996/2017 and COVID/BD/152172/2021 assigned by FCT. This work was developed within the scope of the project CICECO-Aveiro Institute of Materials, UIDB/50011/2020 (DOI: **https://doi.org/10.54499/UIDB/50011/2020**), UIDP/50011/2020 (DOI: **https://doi.org/10.54499/UIDP/50011/2020**) & LA/P/0006/2020 (DOI: **https://doi.org/10.54499/LA/P/0006/2020**), financed by national funds through the FCT/MCTES (PIDDAC). Figures and graphical abstracts were created with **https://BioRender.com**. The support of Professor Ricardo Castro, and

Dr Rui Manadas from UCQFarma is also acknowledged for making DSC, ATR-FTIR, and XRPD facilities available. We also acknowledge Professor Amilcar Ramalho for making the Testo 875 – Infrared camera available.

References

1 H. Sung, J. Ferlay, R. L. Siegel, M. Laversanne, I. Soerjomataram, A. Jemal and F. Bray, *Ca-Cancer J. Clin.*, 2021, **71**, 209–249.
2 R. Stupp, M. Brada, M. J. Van Den Bent, J. Tonn, G. Pentheroudakis, E. Guidelines and W. Group, *ESMO Update Clin. Pract. Guidel.*, 2014, **25**, iii93–iii101.
3 B. Oronsky, T. R. Reid, A. Oronsky, N. Sandhu and S. J. Knox, *Front. Oncol.*, 2021, **10**, 1–10.
4 E. K. Noch, R. Ramakrishna and R. Magge, *World Neurosurg.*, 2018, **116**, 505–517.
5 W. Wu, J. L. Klockow, M. Zhang, F. Lafortune, E. Chang, L. Jin, Y. Wu and H. E. Daldrup-Link, *Pharmacol. Res.*, 2021, **171**, 105780.
6 V. P. Ferrer, V. Moura Neto and R. Mentlein, *Glia*, 2018, **66**, 1542–1565.
7 C. G. Alves, D. De Melo-diogo, R. Lima-sousa and E. C. Costa, *Eur. J. Pharm. Biopharm.*, 2019, **137**, 86–94.
8 A. Li Volsi, C. Scialabba, V. Vetri, G. Cavallaro, M. Licciardi and G. Giammona, *ACS Appl. Mater. Interfaces*, 2017, **9**, 14453–14469.
9 J. Basso, M. Mendes, A. Fortuna, R. Vitorino, J. Sousa, A. Pais and C. Vitorino, *Drug Repurposing in Cancer Therapy*, Elsevier, 2020, pp. 353–393.
10 M. Antoszczak, A. Markowska, J. Markowska and A. Huczyński, *Eur. J. Pharmacol.*, 2020, **866**, 172784.
11 M. Vera, E. Barcia, S. Negro, P. Marcianes, L. Garcia-Garcia, K. Slowing and A. Fernández-Carballido, *Int. J. Pharm.*, 2014, **473**, 518–527.
12 E. Salehifar and S. J. Hosseinimehr, *Drug Discovery Today*, 2016, 1–9.
13 Ł. Uram, J. Markowicz, M. Misiorek, A. Filipowicz-Rachwał, S. Wołowiec and E. Wałajtys-Rode, *Eur. J. Pharm. Sci.*, 2020, **152**, 105439.
14 M. Rudrapal, J. S. Khairnar and G. A. Jadhav, *Drug Repurposing Hypothesis Mol. Asp. Ther. Appl*, 2020, vol. 10, p. 234.
15 K. Margulis, E. A. Neofytou, R. E. Beygui and R. N. Zare, *ACS Nano*, 2015, 9416–9426.
16 N. Sakoguchi-Okada, F. Takahashi-Yanaga, K. Fukada, F. Shiraishi, Y. Taba, Y. Miwa, S. Morimoto, M. Iida and T. Sasaguri, *Biochem. Pharmacol.*, 2007, **73**, 1318–1329.
17 G. Steinbach, P. M. Lynch, R. K. S. Phillips, M. H. Wallace, E. Hawk, G. B. Gordon, N. Wakabayashi, B. Saunders, Y. Shen and T. Fujimura, *N. Engl. J. Med.*, 2000, **342**, 1946–1952.
18 J. L. Roti Roti, *Int. J. Hyperthermia*, 2008, **24**, 3–15.
19 C. Christophi, A. Winkworth, V. Muralihdaran and P. Evans, *Surg. Oncol.*, 1998, **7**, 83–90.
20 M. Mendes, A. Barone, J. Sousa, A. Pais and C. Vitorino, *Nanotheranostics*, Springer, 2019, pp. 363–404.
21 A. Curcio, A. K. A. Silva, S. Cabana, A. Espinosa, B. Baptiste, N. Menguy, C. Wilhelm and A. Abou-Hassan, *Theranostics*, 2019, **9**, 1288.
22 Z. Xu, Y. Zhang, W. Zhou, L. Wang, G. Xu, M. Ma, F. Liu, Z. Wang, Y. Wang and T. Kong, *J. Nanobiotechnol.*, 2021, **19**, 1–11.
23 J. Sun, Y. Li, Y. Teng, S. Wang, J. Guo and C. Wang, *Nanoscale*, 2020, **12**, 14775–14787.
24 Y. Li, T. M. D. Le, Q. N. Bui, H. Y. Yang and D. S. Lee, *Carbohydr. Polym.*, 2019, **226**, 115281.
25 R. Riedel, N. Mahr, C. Yao, A. Wu, F. Yang and N. Hampp, *Nanoscale*, 2020, **12**, 3007–3018.
26 S. Chu and U. Stochaj, *Cancer Drug Resist.*, 2020, **3**, 302.
27 Y. Yu, A. Wang, S. Wang, Y. Sun, L. Chu, L. Zhou, X. Yang, X. Liu, C. Sha, K. Sun and L. Xu, *Mol. Pharmaceutics*, 2022, **19**, 1219–1229.
28 Y. Nakamura, A. Mochida, P. L. Choyke and H. Kobayashi, *Bioconjugate Chem.*, 2016, **27**, 2225–2238.
29 J. I. Hare, T. Lammers, M. B. Ashford, S. Puri, G. Storm and S. T. Barry, *Adv. Drug Delivery Rev.*, 2016, **108**, 25–38.
30 M. Mendes, J. Basso, J. Silva, T. Cova, J. Sousa, A. Pais and C. Vitorino, *Int. J. Pharm.*, 2020, **587**, 119661.
31 M. Mendes, A. Miranda, T. Cova, L. Gonçalves, A. J. Almeida, J. J. Sousa, M. L. C. do Vale, E. F. Marques, A. Pais and C. Vitorino, *Eur. J. Pharm. Sci.*, 2018, **117**, 255–269.
32 J. Basso, M. Mendes, J. Silva, J. Sereno, T. Cova, R. Oliveira, A. Fortuna, M. Castelo-Branco, A. Falcão, J. Sousa, A. Pais and C. Vitorino, *Eur. J. Pharm. Biopharm.*, 2020, **155**, 177–189.
33 M. Mendes, J. Basso, J. Sousa, A. Pais and C. Vitorino, *J. Mol. Liq.*, 2020, 1–7.
34 Y. Han, Y. Zhang, D. Li, Y. Chen, J. Sun and F. Kong, *Int. J. Nanomed.*, 2014, **9**, 4107.
35 B. Gupta, C. S. Yong and J. O. Kim, *J. Pharm. Invest.*, 2017, 1–13.
36 M. Uner, *Pharmazie*, 2006, **61**, 375–386.
37 L. Harivardhan Reddy, K. Vivek, N. Bakshi and R. S. R. Murthy, *Pharm. Dev. Technol.*, 2006, **11**, 167–177.
38 Y.-T. Liao, C.-H. Liu, Y. Chin, S.-Y. Chen, S. H. Liu, Y.-C. Hsu and K. C.-W. Wu, *J. Mater. Chem. B*, 2019, **7**, 4451–4460.
39 B. Seo, K. Lim, S. S. Kim, K. T. Oh, E. S. Lee, H.-G. Choi, B. S. Shin and Y. S. Youn, *Colloids Surf., B*, 2019, **179**, 340–351.
40 L. Lihuang, G. Qiuyan, L. Yanxiu, L. Mindan, Y. Jun, G. Yunlong, Z. Qiang, S. Benqiang, W. Xiumin and L. Liangcheng, *J. Mater. Sci. Technol.*, 2021, **63**, 81–90.
41 G. A. Dichello, T. Fukuda, T. Maekawa, R. L. D. Whitby, S. V. Mikhalovsky, M. Alavijeh, A. S. Pannala and D. K. Sarker, *Eur. J. Pharm. Sci.*, 2017, **105**, 55–63.
42 Z. Li, H. Huang, S. Tang, Y. Li, X.-F. Yu, H. Wang, P. Li, Z. Sun, H. Zhang and C. Liu, *Biomaterials*, 2016, **74**, 144–154.
43 A. R. Rastinehad, H. Anastos, E. Wajswol, J. S. Winoker, J. P. Sfakianos, S. K. Doppalapudi, M. R. Carrick, C. J. Knauer, B. Taouli and S. C. Lewis, *Proc. Natl. Acad. Sci. U. S. A.*, 2019, **116**, 18590–18596.
44 Z. Wang, T. Y. Lee and P. C. Ho, *Nanomedicine*, 2012, **8**, 194–203.
45 H. Hyun, Y. Yoo, S. Y. Kim, H. S. Ko, H. J. Chun and D. H. Yang, *J. Ind. Eng. Chem.*, 2020, **81**, 178–184.

46 F. Branco, J. Cunha, M. Mendes, C. Vitorino and J. J. Sousa, *ACS Nano*, 2024, **18**, 16359–16394.
47 H. Maeda, J. Wu, T. Sawa, Y. Matsumura and K. Hori, *J. Controlled Release*, 2000, **65**, 271–284.
48 J. Li, W. Wang, X. Zhang, H. Yao, Z. Wei, X. Li, X. Mu, J. Jiang and H. Zhang, *RCS Adv.*, 2018, 21316–21325.
49 D. Shajari, A. Bahari, P. Gill and M. Mohseni, *Opt. Mater.*, 2017, **64**, 376–383.
50 A. M. Alkilany, P. K. Nagaria, C. R. Hexel, T. J. Shaw, C. J. Murphy and M. D. Wyatt, *Small*, 2009, **5**, 701–708.
51 J. He, S. Unser, I. Bruzas, R. Cary, Z. Shi, R. Mehra, K. Aron and L. Sagle, *Colloids Surf., B*, 2018, **163**, 140–145.
52 T. S. Hauck, A. A. Ghazani and W. C. W. Chan, *Small*, 2008, **4**, 153–159.
53 L. Wang, X. Jiang, Y. Ji, R. Bai, Y. Zhao, X. Wu and C. Chen, *Nanoscale*, 2013, **5**, 8384–8391.
54 M. Bhamidipati and L. Fabris, *Bioconjugate Chem.*, 2017, **28**, 449–460.
55 A. Kumar, S. Mandal, P. R. Selvakannan, R. Pasricha, A. B. Mandale and M. Sastry, *Langmuir*, 2003, **19**, 6277–6282.
56 J. Gao, X. Huang, H. Liu, F. Zan and J. Ren, *Langmuir*, 2012, **28**, 4464–4471.
57 L. García Fernández and E. Boix i Borràs, Universitat Autònoma de Barcelona, 2013.
58 M. Vukomanovic, M. del Mar Cendra, A. Baelo and E. Torrents, *Colloids Surf., B*, 2021, **208**, 112083.
59 S. Zhang, Y. Li, X. He, S. Dong, Y. Huang, X. Li, Y. Li, C. Jin, Y. Zhang and Y. Wang, *Int. J. Nanomed.*, 2014, 1931–1946.
60 M. R. K. Ali, Y. Wu, Y. Tang, H. Xiao, K. Chen, T. Han, N. Fang, R. Wu and M. A. El-Sayed, *Proc. Natl. Acad. Sci. U. S. A.*, 2017, **114**, E5655–E5663.
61 S. Yao, H.-H. Cai, M. Liu and P.-H. Yang, *Dyes Pigm.*, 2014, **101**, 286–294.
62 J. Tao, Y. Wang, W. Zhai and M. Wang, *J. Adv. Res.*, 2024, **67**, 15–23.
63 M. Mendes, S. Nunes, T. Cova, F. Branco, M. Dyrks, B. Koksch, N. Vale, J. Sousa, A. Pais and C. Vitorino, *Colloids Surf., B*, 2024, **241**, 113983.
64 Y.-P. Jia, B.-Y. Ma, X.-W. Wei and Z.-Y. Qian, *Chin. Chem. Lett.*, 2017, **28**, 691–702.
65 C. Carnovale, G. Bryant, R. Shukla and V. Bansal, *ACS Omega*, 2019, **4**, 242–256.
66 Q. Xia, J. Huang, Q. Feng, X. Chen, X. Liu, X. Li, T. Zhang, S. Xiao, H. Li and Z. Zhong, *Int. J. Nanomed.*, 2019, **14**, 6957–6970.
67 V. Guerrero-Florez, S. C. Mendez-Sanchez, O. A. Patrón-Soberano, V. Rodríguez-González, D. Blach and F. Martínez, *J. Mater. Chem. B*, 2020, **8**, 2862–2875.
68 A. M. Engstrom, R. A. Faase, G. W. Marquart, J. E. Baio, M. R. Mackiewicz and S. L. Harper, *Int. J. Nanomed.*, 2020, **15**, 4091–4104.
69 B. Srinivasan, A. R. Kolli, M. B. Esch, H. E. Abaci, M. L. Shuler and J. J. Hickman, *J. Lab. Autom.*, 2015, **20**, 107–126.
70 Y.-C. Kuo and L.-J. Wang, *J. Taiwan Inst. Chem. Eng.*, 2014, **45**, 755–763.
71 K. B. Johnsen, A. Burkhart, F. Melander, P. J. Kempen, J. B. Vejlebo, P. Siupka, M. S. Nielsen, T. L. Andresen and T. Moos, *Sci. Rep.*, 2017, **7**, 10396.
72 V. M. Pulgar, *Front. Neurosci.*, 2019, **12**, 1019.
73 B. Voth, D. T. Nagasawa, P. E. Pelargos, L. K. Chung, N. Ung, Q. Gopen, S. Tenn, D. T. Kamei and I. Yang, *J. Clin. Neurosci.*, 2015, **22**, 1071–1076.
74 J.-Q. Gao, Q. Lv, L.-M. Li, X.-J. Tang, F.-Z. Li, Y.-L. Hu and M. Han, *Biomaterials*, 2013, **34**, 5628–5639.
75 B. W. Neun, A. N. Ilinskaya and M. A. Dobrovolskaia, NCL Method ITA-1, 2016, 8, 2180–2187.
76 L. Wang and C. Niu, *J. Mater. Chem. B*, 2021, **9**, 4079–4097.
77 C. G. Alves, R. Lima-sousa, D. De Melo-diogo and R. O. Louro, *Int. J. Pharm.*, 2018, **542**, 164–175.
78 S. Mannucci, F. Boschi, B. Cisterna, E. Esposito, R. Cortesi, C. Nastruzzi, E. Cappellozza, P. Bernardi, A. Sbarbati and M. Malatesta, *Int. J. Nanomed.*, 2020, **15**, 1745.
79 M. Xu, G. Li, H. Zhang, X. Chen, Y. Li, Q. Yao and M. Xie, *Drug Delivery*, 2020, **27**, 983–995.
80 J. Li, H. Zeng, Y. You, R. Wang, T. Tan, W. Wang, L. Yin, Z. Zeng, Y. Zeng and T. Xie, *J. Nanobiotechnol.*, 2021, **19**, 1–19.
81 X. Xu, Y. Chong, X. Liu, H. Fu, C. Yu, J. Huang and Z. Zhang, *Acta Biomater.*, 2019, **84**, 328–338.
82 P. Kumar, T. Van Treuren, A. P. Ranjan, P. Chaudhary and J. K. Vishwanatha, *Nanotechnology*, 2019, **30**, 265101.
83 Y. Zhang, M. Huo, J. Zhou and S. Xie, *Comput. Methods Programs Biomed.*, 2010, **99**, 306–314.
84 M. Mendes, J. J. Sousa, A. Pais and C. Vitorino, *Processes*, 2023, **11**, 1–12.
85 R. Yi, H. Wang, C. Deng, X. Wang, L. Yao, W. Niu, M. Fei and W. Zhaba, *Biosci. Rep.*, 2020, **40**, BSR20193314.
86 R. Spellerberg, T. Benli-Hoppe, C. Kitzberger, M. Hageneier, N. Schwenk, Ö. Öztürk, K. Steiger, G. Multhoff, M. Eiber and F. Schilling, *Mol. Ther.*, 2022, **27**, 272–287.
87 P. V. Candelaria, L. S. Leoh, M. L. Penichet and T. R. Daniels-Wells, *Front. Immunol.*, 2021, **12**, 607692.
88 S. Pinel, N. Thomas, C. Boura and M. Barberi-Heyob, *Adv. Drug Delivery Rev.*, 2019, **138**, 344–357.
89 H. Arami, S. Kananian, L. Khalifehzadeh, C. B. Patel, E. Chang, Y. Tanabe, Y. Zeng, S. J. Madsen, M. J. Mandella and A. Natarajan, *Nat. Nanotechnol.*, 2022, **17**, 1015–1022.
90 J. I. Traylor, R. Patel, M. Muir, D. C. de Almeida Bastos, V. Ravikumar, C. Kamiya-Matsuoka, G. Rao, J. G. Thomas, Y. Kew and S. S. Prabhu, *World Neurosurg.*, 2021, **149**, e244–e252.
91 J. F. De Groot, A. H. Kim, S. Prabhu, G. Rao, A. W. Laxton, P. E. Fecci, B. J. O'Brien, A. Sloan, V. Chiang and S. B. Tatter, *Neuro-Oncol. Adv.*, 2022, **4**, vdac040.
92 C. Prieto and I. Linares, *Rep. Pract. Oncol. Radiother.*, 2018, **23**, 474–480.
93 S. Kumari, S. M. Ahsan, J. M. Kumar, A. K. Kondapi and N. M. Rao, *Sci. Rep.*, 2017, **7**, 1–13.